

Monthly Weather Review
Physics-dynamics coupling with element-based high-order Galerkin methods: quasi equal-area physics grid
--Manuscript Draft--

Manuscript Number:	MWR-D-18-0136
Full Title:	Physics-dynamics coupling with element-based high-order Galerkin methods: quasi equal-area physics grid
Article Type:	Article
Corresponding Author:	Adam R. Herrington, M.S., 2011, University of Michigan State University of New York at Stony Brook Stony Brook, NY UNITED STATES
Corresponding Author's Institution:	State University of New York at Stony Brook
First Author:	Adam R. Herrington, M.S.
Order of Authors:	Adam R. Herrington, M.S. Peter H. Lauritzen, PhD Mark A. Taylor, PhD Steve Goldhaber, PhD Brian E. Eaton, PhD Julio T. Bacmeister, PhD Kevin A. Reed, PhD Paul A. Ullrich, PhD
Abstract:	Atmospheric modeling with element-based high-order Galerkin methods presents a unique challenge to the conventional physics-dynamics coupling paradigm, due to the highly irregular distribution of nodes within an element and the distinct numerical characteristics of the Galerkin method. The conventional coupling procedure is to evaluate the physical parameterizations ($\{\text{lem}\{\text{physics}\}\}$) on the dynamical core grid. Evaluating the physics at the nodal points exacerbates numerical noise from the Galerkin method, enabling and amplifying local extrema at element boundaries. Grid imprinting may be substantially reduced through the introduction of an entirely separate, approximately isotropic finite-volume grid for evaluating the physics forcing. Integration of the spectral basis over the control-volumes provides an area average state to the physics, which is more representative of the state in the vicinity of the nodal points rather than the nodal point itself, and is more consistent with the notion of a 'large-scale state' required by conventional physics packages. This study documents the implementation of a quasi-equal area physics grid into NCAR's Community Atmosphere Model with Spectral Elements, and is shown to be effective at mitigating grid imprinting in the solution. The physics grid is also appropriate for coupling to other components within the Community Earth System Model, since the coupler requires component fluxes to be defined on a finite-volume grid, and one can be certain that the fluxes on the physics grid are indeed, volume-averaged.



Click here to access/download

Cost Estimation and Agreement Worksheet
Journals_CEAW.pdf

General comments and common themes:

One of the main results of this study is that the implementation of a finite-volume physics grid in CAM-SE-CSLAM leads to a significant reduction in grid imprinting compared with CAM-SE. A point that was not made so clear throughout the paper is that the overall solutions between CAM-SE and CAM-SE-CSLAM are more similar than dissimilar. This is generally true, but not in an absolute sense. In some cases, like the aqua-planets, the dependency of the solution on proximity to element boundaries is more subtle. The Held-Suarez simulations, however, indicate that numerical noise associated with flow over rough topography may not be so subtle and can result in significant climatological errors. This point has been elaborated in various places throughout the manuscript.

A common request from the reviewers was to include the results of another supporting figure, whether from one of the simulations already performed, or from an entirely new experiment. While we address the specific concerns of the reviewers individually, the following steps were taken to satisfy this common concern:

(1). A lower complexity test-case is introduced, the moist baroclinic wave test-case of DCMIP 2016. The baroclinic wave test is used to drive the Terminator “toy”-chemistry test-case, in order to assess whether tracer mass is conserved, as stated in the methods section. Two figures are introduced. Figure 6 indicates that the differences in baroclinic wave solution between CAM-SE and CAM-SE-CSLAM are small. Figure 7 indicates that the tracer mass is conserved in CAM-SE-CSLAM, but not CAM-SE.

(2) We have included a plot of the climatological, zonal-mean precipitation rate in the CAM-SE and CAM-SE-CSLAM aqua-planets, to draw attention to the fact that the mean states are very similar (Figure 8).

(3) A more complex, AMIP configuration is introduced. Two additional figures are included. Figure 11 focuses on grid imprinting in regions of rough topography, in CAM-SE and CAM-SE-CSLAM, and Figure 12 compares the global precipitation field in these runs to CAM-FV and the GPCP gridded dataset.

Reviewer Comments for ‘Physics-dynamics coupling with element-based high-order Galerkin methods: quasi equal-area physics grid’

Reviewer 1

The article describes a new physics-dynamics coupling procedure in a model using the element-based Galerkin methods which have the irregular distribution of nodes within an element. Because DSS operations force the solution to have C0 continuity, strong grid-scale forcing at the element boundaries exacerbates discontinuity. So that the authors introduce new physics-dynamics coupling method using an entirely separate finite-volume grid for evaluation the physics forcing in spectral element model.

The background and methodology are well explained and the results suggest some useful to relieve grid imprinting (enhance the stability) although the present study concerns only climatological ideal tests (year-long aqua-planet and Held-Suarez test). Some comments to the manuscript are as follows.

(1) The manuscript seems to explain why and how the grid-imprinting emerge, rather than represents how much improvement in simulation results. Since the results of CAM-SE-CSLAM using the separated physics grid are very limited to represent its impact on the simulation using three figures (Figs 3, 6, and 7), it would be necessary to carry out other ideal cases (such as DCMIP idealized TC case) or real cases, and to compare the simulation to CAM-FV which is conceptually suitable to take as a reference.

We agree with the reviewer, that another test-case may be a welcome addition. There are three moist physics test cases used in DCMIP2016. The only test case where an approximate reference solution has been introduced, I think, is a measure of the uncertainty in the high resolution reference solution of the moist baroclinic wave test case, published in Lauritzen et al. (2018). Lauritzen et al (2018) provides a measure of the uncertainty in the reference through defining an L2 difference norm between two reasonably converged solutions, using two different dynamical cores: CAM-FV 0.25 degree and CAM-SE 0.25 degree. We have ran the baroclinic wave test, and included a figure of the L2 difference between CAM-SE and CAM-SE-CSLAM, and have overlain the Lauritzen et al. (2018) uncertainty in the reference solution. The L2 difference norm between CAM-SE and CAM-SE-CSLAM lies under the uncertainty in the reference solution. This supports the notion that the overall solutions between the two models are more similar than dissimilar.

From a larger-scale perspective, away from the grid-scale, CAM-SE and CAM-SE-CSLAM have very similar solutions. This can be seen by looking at the contour plot of the mean physics tendencies in the aqua-planets (Figure 9), where the large scale structures look very similar in the two models. To emphasize this point, that the large-scale mean state is not very sensitive to the separate physics grid, we've added a plot of the climatological, zonal mean precipitation rate

in the aqua-planets (Figure 8), to emphasize the similar means states between the two models (discussion beginning at Line 312).

In response to the reviewer, we have included an analysis of a suite of AMIP-type simulations, using CAM-SE, CAM-SE-CSLAM and CAM-FV, in order to help identify spurious precipitation in the simulations. These results are provided in the subsection “AMIP type simulations.” As the reviewer alluded to, there is no absolute truth to evaluate the solutions against. The GPCP dataset and CAM-FV were cautiously used to guide our interpretations.

(2) Since the extrema induced by strong physics forcing at the element boundaries in CAM-SE results in the grid-imprinting, the comparison between the simulations of ne45np3 and ne30np4, which have same DOF, might demonstrate another important feature. Could it be possible that the increasing number of the element boundaries make more grid-imprinting? In addition, because the control volumes around the GLL quadrature point of np3 will be more similar to those of pg2 than np4 to pg3, it could be interesting to comparison of simulation using np3 to that using pg2.

We share the reviewers curiosity on how the imprinting is influenced by different quadrature node configurations. There are many interesting avenues to explore, and in fact, we have a current study in progress exploring the advantages of pg2 over pg3, when the quadrature nodes are np4. It is possible that using np3 quadrature nodes might result in less irregular sampling when mapping to a pg3 physics grid at the possible expense of less higher order of accuracy (at least for smooth problems). This is beyond the scope of this manuscript.

(3) Separation of dynamic and physics grid means that grid-point resolution may be different between dynamics and physics. The volume-averaged physics forcing within an element is sensitive (or insensitive) to the physics resolution?

Generally, we think yes, that the volume average physics forcing is sensitive to the physics grid resolution. A follow-up question is then, how sensitive? We address this more narrowly in our upcoming paper on pg2, of which we now mention in the conclusions (beginning at line 453)

(4) It is hard to distinguish the difference between bottom panels (for Himalayas region) in Fig. 7 although the description in the manuscript. So it needs to be revised.

We have added circles to the plot to draw the reader towards the relevant features.

(5) In the figures, panel identifiers (e.g., (a), (b), and (c)) are omitted in the figures and should be described in the manuscript as well.

These have been added.

Reviewer 2

This work discusses the a new method to interface the spectral element dynamics core and the control–volume based physics parameterizations in the Community Atmosphere Model (CAM) which simplifies the physics mesh representation and addresses well known issues with grid imprinting, a current well–known problem in finite–element solvers. Although the study focuses on CAM, the results could easily be extended to any atmospheric model which uses a finite element framework to solve the dynamics, thus this work is relevant to a broad audience of multi–physics modelers.

This work is an important contribution to the field and should be published. That being said, there are a number of comments that I have given below that should be addressed. Over all the science is good and the results are important, however the points of the manuscript could be made more clearly and succinctly. I would recommend this paper for publication provided that the authors can address the comments I have given below.

1 Introduction

The introduction contains a lot of discussion and arguments that would seem better suited for a separate section on motivations (or something like that). For example 4 out of 8 figures are introduced and discussed in the introduction. This causes the manuscript to introduce simulation results before discussing the details of how the model runs, or even the parameters of the model run. There is a paragraph on an aqua–planet simulation with no details on the model setup parameters, these details are not discussed until a later section. Another option would be to include some of the Introduction discussion in the Methods section (for example much of the second–to–last paragraph).

These points are well taken. We have moved the latter parts of the Introduction into a new section titled “The Quadrature Node Problem.” It is in that section that we introduce the details of the aqua–planet runs, which the reviewer rightfully points out was not detailed until later on in the paper. The figures are now distributed more evenly among the sections.

1. Lines 57–59: The authors should also mention that the DOE E3SM v1 model exclusively uses a high–order Galerkin method (Similar to the CAM–SE).

No problem, we have cited the url since we don't believe that any definitive documentation has been published yet (<https://e3sm.org>).

2. Lines 62–67: The authors discuss finite difference and finite volume approaches, could they also include any examples of models that actually use these approaches?

Absolutely, inserted citations Lin (2004) for FV, Suarez (1983) for FD method (UCLA GCM) at Lines 64 ,67.

3. Line 72: Could the authors briefly describe the differences between these types of grids or maybe just mention different models that use these different mesh approaches?

Certainly. An additional sentence has been added beginning at Line 74.

4. Lines 78–79: maybe $np = 4 \times 4$ and $np = 8 \times 8$ quadrature points, or a different way to say this. From the sentence it seems like there are 4 and 8 quad-points respectively, when there are actually 16 and 64 respectively.

We agree the notation can be confusing, but would like the np's and pg's to maintain their 1D meaning. We would rather it be changed to, e.g., $np \times np = 4 \times 4$, and have done so, assuming the reviewer does not object.

5. Line 79–80: “Both grids have the same average resolution on the sphere (due to different number of elements)”, what does this mean? It is not clear in this context what is meant by average resolution, is this average element-wise resolution, spectral resolution? I think the authors mean that both grids have the same average physics control volume resolution, 7.5 degrees. This is not exactly true, ne4np4 has $360/(4 * 4 * 3) = 7.5^\circ$ and ne2np8 has $360/(4 * 2 * 7) = 6.43^\circ$ resolution.

The reviewer is correct, that both grids do not have the same average resolution on the sphere. We have removed this problematic statement and thank the reviewer for their close attention to detail.

6. Line 81: Is there a better way to say “less equi-distant”? Maybe something like, the spectral resolution in the ne2np8 mesh leads to more variance in the distance between GLL quadrature points on an individual element. A quick calculation shows that the range of GLL distances in the ne4np4 mesh is $(6.22^\circ, 10.06^\circ)$ and for the ne2np8 mesh they are $(2.89^\circ, 6.3^\circ, 8.6^\circ, 9.42^\circ)$.

We agree this point could be made more clear, and have used the reviewers suggested wording (Line 83), “...the greater variance in distance between GLL quadrature points within an element.”

7. Lines 99–102: What resolution, what order elements, how long, what timestep? The authors discuss the results of this aqua–planet simulation without giving any details about the run itself.

This has been addressed in the new section “The Quadrature Node Problem,” beginning at Line 112.

8. Line 101: Why ω ? From reading the manuscript it seems like ω is a variable that shows the diversity of solution based on GLL point location clearly and is thus a good candidate for the

study, but this should be made more explicit in the manuscript.

We agree, that our rationale for using omega should be made explicit in the text. Omega is an excellent proxy for divergent modes, the magnitude of which is larger at the element boundaries due to the C0 continuous pressure gradients. A justification has been inserted beginning at Line 131.

9. Line 102, Figure 3: The second panel (the right panel) of this figure is not referenced until later in the manuscript. It would be less confusing what the references to figure 3 are if the authors included an (a) and (b) designation.

We agree this would make it easier to reference. We have added (a) and (b) to figure 3, and the reference to Figure 3 has been taken out of the Introduction, and put into the “Quadrature Node Problem” section.

10. Line 126: What does “quasi–equal“ area mean? The authors should point out that having every control volume have equal area is unrealistic, so quasi–equal area is the closest we can get. Do the authors have any sense of how much variation in control volume area there is over the mesh?

Since the control volumes divide up the element using equi-angular coordinate lines parallel to the equi-angular element boundaries, one measure of anisotropy is the ratio of the largest to smallest element area on the grid. This ratio appears to range from about 1.3 - 1.4 for typical climate model grid resolutions (ne16->ne120).

We have decided against making any claims about whether it is possible to construct a truly equal area grid, but have decided to emphasize that we specifically choose a equi-angular physics grid, in the methods section, beginning at line 175.

2 Methods

As a general comment, the authors do a good job of discussing the importance of tracer mass conservation when mapping from the GLL based mesh to the PG quasi-equal area control volume mesh, but there does not seem to be any verification that the mass is conserved. Has there been a study that verified that this approach is mass conserving? If not, did the authors keep track of the tracer mass on the dynamics mesh and then compare this with the tracer mass after the interpolation onto the PG mesh?

Lauritzen et al. (2017) shows the results of the Terminator “toy” test, indicating that CAM-SE-CSLAM does conserve tracer mass to within machine precision, while CAM-SE does not.

This study is different, in the sense that we are adding moisture and moist physics to CAM-SE-CSLAM via the introduction of the physics grid. In response to the reviewers comment, we have decided to include the results of the Terminator test case, for CAM-SE and CAM-SE-CSLAM, initialized with the moist baroclinic wave test case, described in a new section “Moist baroclinic wave”. The test reveals that CAM-SE does not preserve tracer mass and linear correlations, while CAM-SE-CSLAM does to machine precision (Figure 7).

1. Lines 154–158: Would this approach still be possible if the default vertical coordinate system was used instead of a dry–mass coordinate system? What complications would be expected?

See response to comment 5, below.

2. Lines 169–170 and 204–206: Could the authors briefly discuss the potential issues with not including these properties, why was it decided that they would be neglected at this time?

We have elaborated on why we have neglected conserving total energy and AAM (Lines 203–212).

3. Line 176: How many quadrature points? If each integral represents a control volume integration isn’t it true that any given physics control volume could have at most 4 GLL points associated with it (for np=4 and pg=3)? If less quad points are used doesn’t that introduce an integration error? Or is it that each control volume is broken into a set of local quadrature points?

There should not be an integration error, since we are integrating the polynomial basis exactly using the quadrature rules. This was shown in Lauritzen et al (2017), in the mapping section, and has been made explicit in the text (Line 219).

4. Line 179: “and then transformed”

Done.

5. Lines 194–196: How do you address the fact that by default CAM–SE passes the tracer state (not tendencies) to the dynamics core? As a follow–up, which physics/dynamics coupling paradigm is used for these runs? Sequential–Update, Sequential–Tendency a mixture of Seq. Update and Seq. Tendency? What impact, if any, do you expect the coupling paradigm to have on the grid imprinting phenomenon?

Thank you for pointing out this important point!

The consistent coupling between the SE continuity equation for air and the continuity equation for tracers (solved with CSLAM) is much more consistent in a dry-mass coordinate as explained in the following. In a dry-mass formulation CSLAM transports water tracers while SE solves the

continuity equation for dry air. The two are consistently coupled by making sure that if a tracer has a value of 1 (in which case CSLAM predicts the evolution of dry air mass) then the CSLAM dry mass field is identical to the SE dry mass field integrated over CSLAM control volumes (how this is done is explained in detail in Lauritzen et al., 2017). Had one used a moist vertical coordinate, then this coupling between SE and CSLAM would be complicated by the fact that water tracers would implicitly be predicted by SE through solving the continuity equation for moist air mass (using a moist vertical coordinate).

That said, if SE and CSLAM solutions for water vapor transport do not differ much then the methodology presented in this paper should still work. One just has to make sure that moisture values in SE are periodically overwritten by CSLAM moisture values (as is done in the current setup). Description added to manuscript.

A small section on the time-splitting has been included, beginning at Line 276. While we do not speculate on splitting methods other than sequential-update, a discussion of how the sequential-update is distributed over a time-step for the different models, and why, is included.

6. Line 206: “mapped from the physics grid”

Done.

7. Line 221: “it was found that it is (a) important ...”

Done.

8. Line 225–226: What stencil did you use? One element to either side? If you need a stencil doesn’t this require communication across computational cores when an element boundary is shared by more than one core? If so, this should be mentioned.

CSLAM with $CFL < 1$ requires 3 cell average values halo. SE only needs to communicate GLL point on the boundary of an element. SE communicates every Runge-Kutta step and twice every hyperviscosity subcycling step. CSLAM only communicates every CSLAM time-step. So for tracer advection SE communicates 30 times per physics time-step (once per Runge-Kutta step and there are 3 steps; last Runge-Kutta step hyperviscosity is applied which is 2 communications - the limiter has a couple of min-max communications not accounted for here) and CSLAM communicates twice. So CSLAM communicates 15 times less frequently compared to SE but the halo is 8 times larger than SE.

Despite the wide halo (compared to SE) CSLAM still exhibits strong scaling. See Figure 15b in Lauritzen et al. (2017).

9. Lines 221–233: The response to point (a) is explicitly discussed in this paragraph, but the response to point (b) isn't clearly stated as such.

This paragraph has been clarified and expanded into two paragraphs beginning at Line 256. The first paragraph corresponds to point (b), the second (a).

10. Line 231–233: The word “hence” doesn't make sense in this context. It is not clear what other approaches were considered, why they were deficient and why tensor–cubic interpolation was the best way forward.

This section has been reworded through addressing the previous comment.

3 Results

1. Lines 239–240: It is strange to say a plot similar to figure 3 is constructed in figure 3. This would be more clear if the authors added an (a) and (b) to the subfigures, then it would be that a plot similar to 3a is given in 3b.

Done.

2. Lines 247–248: In the previous paragraph and in figure 3 the variable is ω , here (for Figure 6) we are looking at temperature tendencies. The switch to temperature isn't mentioned anywhere in this paragraph leaving the reader to assume we are still talking about ω . Is there a reason that figure 3 uses ω and figure 6 uses temperature tendencies?

Yes there is a reason, but not clearly stated in the text. We believe ω to be sensitive measure of grid imprinting in the dynamical state, which we have clarified in the Quadrature Node Problem section.

Line 335: “Since the state is approximately independent of in-element location, it follows that the physics forcing, which is evaluated from the dynamical core state, may be expected to also show an improvement in grid-imprinting.”

The beginning of the next paragraph then starts with “The low-level, mean and variance of the temperature tendencies from the physics, on the GLL grid, ft , in the two simulations are shown in Figure 9.”

The flow from talking about the dynamical core state to physics tendencies is now more clear.

4 Figures

1. Figure 2: This is a very long caption. For a caption to need to be this long it makes more sense for this description to be included in the body of the paper with a shorter concise caption

here.

Yes, it is a very long caption. We agree with the reviewer and have moved much of the caption into the text, beginning at Line 112.

2. Figure 3: See previous comments.

Subheaders (a) and (b) have been added to Figure 3.

3. Figure 4: It appears from the figure that control volumes have three possible shapes; triangle (at cubic face interfaces), quadrilateral and pentagonal. Is it true that some control volumes in the default model can have 5 sides? How are the control volume vertices calculated?

We have included a description of how the control volume grid is constructed, beginning at Line 144:

“...One approach to construct this grid is to decompose each spectral element into $$(np-1) \times (np-1)$$ subcells and then take the dual grid of this subcell grid. For cubed-sphere meshes, this dual grid will have a control volume associated with each quadrature point. These control volumes will be triangles for the cube corner quadrature points and quadrilaterals for all remaining quadrature points. Newton iteration can then be used to adjust the corners of these control volumes so that their spherical area exactly match the Gaussian weight multiplied by the metric term (these weights are used for integrating the basis functions over the elements and can therefore, in this context, be interpreted as areas). For cubed-sphere meshes, the Newton iteration can be replaced by a direct method if some of the quadrilaterals are replaced by pentagons giving additional flexibility in matching the spherical area to the quadrature weights. Such a dual grid is shown in Fig 4. This approach is used for cubed-sphere grids in the NCAR CESM, ...”

Reviewer 3

The manuscript outlines a procedure for coupling finite difference (or finite volume) physics parametrizations with an element-based high order Galerkin dynamical core. In particular, the method differs from previous strategies in which physics schemes interact with the dynamics representation at each quadrature point (nodal point) of the finite element representation. In this work, the physics 'grid' is decoupled from that determined by the quadrature points and, moreover, the authors choose to use a 'quasi equal-area' physics grid.

The motivation and method is generally well explained, though I would like the authors to provide a little more background to the model formulation and additional results showing the impact of the application of the method. With regard to the former, the minor comments below include a number of questions that are pertinent to the coupling aspects and that, while they could mostly be found in the cited literature, would benefit the paper from reiterating here.

Major Comments:

1 The results section quite rightly concentrates on the grid imprinting aspects of the method. However, the authors are careful to consider and specify a number of important properties for the mappings. Although some reference is made in the text to the successful recovery of these properties, I think there should be some additional evidence provided for each of these. Some of this could possibly come from further budget analysis of the aquaplanet simulations, but better demonstrations might be provided using one or two idealized tests that are described in the literature (e.g. Lauritzen et al 2015, 'The terminator "toy" chemistry test: a simple tool to assess errors in transport schemes').

We agree with the reviewer that an additional result supporting our design choices should be provided. As suggested by the reviewer, the results of the Terminator "toy" chemistry test is now included in this work (Figure 7). The Terminator test indicates that tracer mass is conserved to within machine precision in CAM-SE-CSLAM, and that it is not conserved in CAM-SE. The moist baroclinic wave test, which the terminator test uses to advect tracers, was also analyzed to show that the overall difference in solution between CAM-SE and CAM-SE-CSLAM are small (Figure 6). Figures 6 and 7 are discussed in a new section "Moist baroclinic wave," beginning at Line 288.

An additional aqua-planet figure has been included, depicting the zonal average climatological precipitation rates, to support the notion that the mean states are very similar in CAM-SE and CAM-SE-CSLAM.

Two additional figures highlighting grid imprinting over topography are included from an AMIP-type simulation (Figures 11 and 12), and we have introduced a new section with the same name (beginning at Line 383).

Minor Comments:

2 The mappings between the physics and dynamics components focus on the horizontal aspects, it would be useful for the authors to briefly expand on the details of the vertical coordinate and grid/mesh. In particular: is there any staggering of physics variables in the vertical?; are fields continuous/discontinuous in the vertical?; I don't believe the fields are high order in the vertical, but it would be good to state this (or otherwise). This is very important to understand from a physics-dynamics coupling perspective, so think it should be reiterated here.

Two sentences have been inserted beginning at Line 189, briefly describing the vertical coordinate system. The vertical discretizations are low-order.

3 Related to this, it should be clarified that the dimensionally split interpolation is horizontal only and no mapping is done in the vertical.

Dimensionally split interpolation is only in the horizontal, and this point has been inserted at Line 251.

4 Line 158/202: In your required properties you state 'linear correlation preservation'. Please could you expand on what this means and why it is important?

The terminator test can verify whether linear correlations are preserved. For example, if a reactive species crosses the terminator, it dissociates into another species. Let's say the original reactive species is driven negative, and the product species obviously is driven positive. To deal with negative tracer values, lets say we clip the negative values (or a limiter chops off more of the negatives concentrations than it does to the product species concentrations). Then the total tracer mixing ratio is not conserved, and there is now a disproportionate amount of the product species relative to the original reactive species. Linear correlations between these two species are not preserved.

5 Line 175: 'The integrals are numerically computed using the GLL quadrature rule'. This is a bit ambiguous given that you're now integrating over a subdomain of the element. Please clarify.

Integrating the basis over control volumes within the element is exact to within machine precision. This was shown in Lauritzen et al (2017), and has been referenced at Line 219.

6 Line 239: 'A plot similar to Figure 3...'. This is Figure 3 isn't it?

Yes, the wording is ambiguous here. We have added labels (a) and (b), so the new text reads "A plot similar to Figure 3a..."

7 Figure 3: I don't dispute the conclusions drawn from this figure, but I have two comments on

this figure:

This figure has been changed. The right plot (now 3b) has been divided into three categories, instead of nine. This was done to create a more ‘apples to apples’ comparison between the two plots, recognizing also that there are three classes of nodal distributions making up the 3x3 physics grid.

- Am I right in thinking there are more data values incorporated in the statistics for each curve for the left plot than those on the right (I.e. 4x for ‘corners’ and ‘interior’, 8x for ‘edges’) making it difficult to compare the tails of the distributions. It would be useful to note that for the readers’ benefit.

Yes, the reviewer is correct. We believe this issue has been addressed with our new sampling in figure 3b. Also note that due to the overlapping nodes, the number of unique nodes within an individual elements is 1x for ‘corners’, and 4X for ‘interior’ and ‘edges.’

- If you overlay the two plots, you will see that there is a decrease in the fraction of values greater than ~0.5 Pa/s. It would be useful to show an overlaid plot and acknowledge this impact - presumably the result of a systematic smoothing and thus damping through the interpolation.

The reviewer is right. We suspect that perhaps the different sampling sizes in old Fig. 3a vs. 3b may be playing a role. The new Figure 3b generally shows that the magnitudes of the three categories of pg3 omega, are most similar to the magnitudes of the interior and edge nodes in np4, in Figure 3a (save for the extreme tails).

8 Line 269: re fig 7: ‘data are plotted on the control volume grid’. Is this contradictory to the caption, since the right plot is on the physics grid?

We thank the reviewer for pointing out this source of confusion. The control volume grid refers to the grid where the physics is computed, whether CAM-SE or the finite-volume physics grid in CAM-SE-CSLAM. We realize this can be confusing, and so have changed the wording, beginning at Line 360.

9 Fig 7: I think it would be helpful to have a difference plot between left and middle in order to elucidate the removal of the topographic grid imprinting.

In response to this comment and another reviewer’s concern, we have added circles to the problem regions of interest described in the text, to more clearly draw the reader towards the features of interest.



1 **Physics-dynamics coupling with element-based high-order Galerkin**
2 **methods: quasi equal-area physics grid**

3 Adam R. Herrington*

4 *School of Marine and Atmospheric Sciences, Stony Brook University, Stony Brook, New York,*
5 *USA.*

6 Peter H. Lauritzen

7 *Climate and Global Dynamics, National Center for Atmospheric Research, 1850 Table Mesa*
8 *Drive, Boulder, Colorado, USA.*

9 Mark A. Taylor

10 *Sandia National Laboratories, Albuquerque, New Mexico, USA.*

11 Steve Goldhaber, Brian E. Eaton and Julio T. Bacmeister

12 *Climate and Global Dynamics, National Center for Atmospheric Research, 1850 Table Mesa*
13 *Drive, Boulder, Colorado, USA.*

14 Kevin A. Reed

15 *School of Marine and Atmospheric Sciences, Stony Brook University, State University of New*
16 *York, Stony Brook, New York.*

17 Paul A. Ullrich

¹⁸ Department of Land, Air and Water Resources, University of California, Davis, California, USA.

¹⁹ *Corresponding author address: Adam R. Herrington, School of Marine and Atmospheric Sciences, Stony Brook University, Stony Brook, New York, USA.

²⁰ E-mail: adam.herrington@stonybrook.edu

ABSTRACT

Atmospheric modeling with element-based high-order Galerkin methods presents a unique challenge to the conventional physics-dynamics coupling paradigm, due to the highly irregular distribution of nodes within an element and the distinct numerical characteristics of the Galerkin method. The conventional coupling procedure is to evaluate the physical parameterizations (*physics*) on the dynamical core grid. Evaluating the physics at the nodal points exacerbates numerical noise from the Galerkin method, enabling and amplifying local extrema at element boundaries. Grid imprinting may be substantially reduced through the introduction of an entirely separate, approximately isotropic finite-volume grid for evaluating the physics forcing. Integration of the spectral basis over the control-volumes provides an area average state to the physics, which is more representative of the state in the vicinity of the nodal points rather than the nodal point itself, and is more consistent with the notion of a ‘large-scale state’ required by conventional physics packages.

This study documents the implementation of a quasi-equal area physics grid into NCAR’s Community Atmosphere Model with Spectral Elements, and is shown to be effective at mitigating grid imprinting in the solution. The physics grid is also appropriate for coupling to other components within the Community Earth System Model, since the coupler requires component fluxes to be defined on a finite-volume grid, and one can be certain that the fluxes on the physics grid are indeed, volume-averaged.

43 **1. Introduction**

44 An increasing number of numerical methods publications in the atmospheric science literature
45 concern transport, shallow-water, and three-dimensional models employing element-based high-
46 order Galerkin discretizations such as finite-element and discontinuous Galerkin methods (for an
47 introduction to these methods see, e.g., ???). Some global models based on Galerkin methods
48 have reached a level of maturity for which they are being considered for next generation climate
49 and weather models due to their inherent conservation properties, high-order accuracy (for smooth
50 problems), high parallel efficiency, high processor efficiency, and geometric flexibility facilitating
51 mesh-refinement applications. NCAR’s Community Atmosphere Model (CAM; ?) offers a dy-
52 namical core based on continuous Galerkin finite elements (?), referred to as CAM-SE (CAM
53 Spectral Elements; ???). CAM-SE is, in particular, being used for high resolution climate model-
54 ing (e.g., ???) and static mesh-refinement applications (e.g., ?????). Other examples of models
55 based on high-order Galerkin methods that are being considered for ‘operational’ weather-climate
56 applications are ?, ?, ? and **the Energy Exascale Earth System Model (<https://e3sm.org/>)**.

57 Assumptions inherent to the physical parameterizations (also referred to as *physics*) require
58 the state passed by the dynamical core represent a ‘large-scale state’, for example, in quasi-
59 equilibrium-type convection schemes (??). In finite-volume methods (e.g., ?), one may think
60 of the dynamical core state as the average state of the atmosphere over a control volume, and for
61 resolutions typical of climate simulations is entirely consistent with the notion of a ‘large-scale
62 state’. For finite-difference methods (e.g., ?) the point value is thought of as representative for the
63 atmospheric state in the vicinity of the point value and one can usually associate a volume with
64 the grid-point. Hence the physics grid (the grid on which the state of the atmosphere is evaluated
65 and passed to physics) and the dynamics grid (the grid the dynamical core uses) coincide. Having

the physics and dynamics grids coincide is obviously convenient since no interpolation is needed
(which could disrupt conservation properties) and the number of degrees of freedom on both grids
is exactly the same.

For the regular latitude-longitude, cubed-sphere and icosahedral grids the distance between the
grid-points is gradually varying for finite-volume/finite-difference discretizations. Examples of
models that use these grids are CAM-FV (latitude-longitude grid, [?](#)), FV3 (cubed-sphere grid, [?](#))
and ICON (icosahedral grid, [?](#)). For high-order element-based Galerkin methods, the dynamical
core grid is defined by the quadrature points. In CAM-SE, these are the Gauss-Lobatto-Legendre
(GLL) quadrature nodes. A unique aspect of the high-order quadrature rules is that the nodes
within an element are located at the roots of the basis set, which may be irregularly spaced. For
example, Figure 1 shows GLL points on an individual element of a cubed-sphere grid for degree
3 ($np \times np = 4 \times 4$ quadrature points) and degree 7 ($np \times np = 8 \times 8$ quadrature points) Lagrange
polynomial basis used in CAM-SE. The higher the order of the quadrature rule, the greater variance
in distance between GLL quadrature points within an element. GLL quadrature points cluster near
the edges and, in particular, the corners of the elements.

The resolved scales of motion are not determined by the distance between quadrature nodes,
but rather the degree of the polynomial basis in each element. The nodes may be viewed as ir-
regularly spaced samples of an underlying spectrally truncated state. From this perspective, one
might expect the nodal solutions to be independent of location within an element. While the in-
terior quadrature nodes are C^∞ in CAM-SE (i.e. the basis representation is infinitely smooth and
all derivatives are continuous), the smoothness of boundary nodes are constrained by the need to
patch neighboring solutions together to form the global basis set, an operation known as the direct
stiffness summation (DSS; [??](#)). The DSS operation is attractive because it allows for high-order
accuracy with minimal communication between elements, but degrades the solution to C^0 at el-

ement boundaries (i.e., all derivatives are discontinuous). Through evaluating the physics at the nodal points, strong grid-scale forcing or oscillatory behavior near an element boundary may exacerbate the discontinuity, and our initial expectation, that the nodal solutions are independent of within-element location, is unlikely for non-smooth problems, e.g., the presence of rough topography or moist physics grid-scale forcing.

It is the purpose of this paper to document the implementation of an entirely separate, quasi-equal area finite-volume physics grid into CAM-SE. The use of a separate physics grid is not entirely unheard of; prior studies have utilized the infrastructure developed for global-spectral transform methods to experiment with different physics grids (???). In our framework, the dynamical core state is integrated over control volumes to provide a volume averaged state to the physics, thereby minimizing the influence of any one particular nodal value on the physics forcing. Section 2 provides a thorough explanation of how grid imprinting manifests in high-order Galerkin methods for non-smooth problems. The implementation of the physics grid configuration into CAM-SE is presented in Section 3. Results from a hierarchy of idealized model configurations are presented in Section 4, illustrating the physics grid is effective at mitigating undesirable grid imprinting in the solution. Section 5 contains a discussion of results and concluding remarks.

2. The Quadrature Node Problem

Figure 2 is a schematic illustrating in one-dimension how grid-imprinting is enabled by the physics, when the dynamical core is built using high-order Galerkin methods. The schematic depicts a time-step, starting from smooth initial conditions (Figure 2a), and subsequently advancing the dynamics one Runge-Kutta time-step (Figure 2b). Since the boundary nodes of adjacent elements overlap one-another, there are now two solutions for each boundary node. The DSS operator, effectively a numerical flux applied to the element boundaries such that overlapping nodal

values agree, is applied (Figure 2c), rendering the solutions at element boundaries C^0 ; less-smooth than neighboring C^∞ interior nodes. An element boundary discontinuity may be exacerbated if, e.g., the physics updates the state at an element boundary (Figure 2d,e), resulting in characteristically tighter gradients on the boundary nodes compared to if the physics forcing were applied to an interior node (Figure 2g,h).

To test the degree to which nodal solutions depend on within-element position, an aqua-planet simulation (??), which consists of an ocean covered planet in perpetual equinox, with fixed, zonally symmetric sea surface temperatures idealized after the present day climatology, is carried out using CAM-SE, using CAM, version 4 physics (CAM4; ?) and run for one year. The nominal low resolution *ne30np4* grid is used, pertaining to an average equatorial grid spacing of 111.2km. The probability density distribution of the upward vertical pressure velocity (ω), conditionally sampled based on three categories - ‘interior’, ‘edge’ and ‘corner’ nodes - is provided in Figure 3a. The motivation for assessing noise in the ω field comes from its connection with the atmosphere’s divergent modes, as follows from the continuity equation in pressure coordinates. These modes are in turn sensitive to the within-element inhomogeneity of the pressure gradient that emerges from high-order Galerkin methods. There is an apparent dependence on nodal location, with interior nodes being characteristically sluggish, and corner and edge nodes having systematically larger magnitude vertical motion. This behavior is consistent with the smoothness properties of the different nodal locations, with discontinuous pressure gradients resulting in greater vertical motion at edge and corner nodes. The main division of solutions shown in Figure 3a is primarily between whether a node is, or is not situated on an element boundary, and is a nuanced signature of high-order element-based Galerkin methods for non-smooth problems.

If the conventional physics-dynamics coupling paradigm is applied to CAM-SE, then the physics are to be evaluated at the GLL nodes, and a volume associated with the quadrature point should

be defined. One approach to construct this grid is to decompose each spectral element into $(np - 1) \times (np - 1)$ subcells and then take the dual grid of this subcell grid. For cubed-sphere meshes, this dual grid will have a control volume associated with each quadrature point. These control volumes will be triangles for the cube corner quadrature points and quadrilaterals for all remaining quadrature points. Newton iteration can then be used to adjust the corners of these control volumes so that their spherical area exactly match the Gaussian weight multiplied by the metric term (these weights are used for integrating the basis functions over the elements and can therefore, in this context, be interpreted as areas). For cubed-sphere meshes, the Newton iteration can be replaced by a direct method if some of the quadrilaterals are replaced by pentagons giving additional flexibility in matching the spherical area to the quadrature weights. Such a dual grid is shown in Figure 4. This grid is used in the NCAR CESM (Community Earth System Model) coupler for passing states between ocean, atmosphere and land components since the current remapping method is finite-volume based and therefore requires control volumes (it is noted that methods exist that do not require control volumes for conservative interpolation, e.g., ?). Hence the components ‘see’ an irregular atmospheric grid. Similarly, the parameterizations in the atmosphere ‘see’ a state that is anisotropically sampled in space (see Figure 1 and 5 in ?).

The quadrature grid in element-based Galerkin methods is defined to perform mathematical operations on the basis functions, e.g., computing gradients and integrals, rather than evaluating the state variables for physics-dynamics coupling. One may argue that it would be more consistent to integrate the basis functions over quasi-equal area control volumes within each element and pass those control volume average values to physics rather than irregularly spaced quadrature point values. In this case when integrating basis functions over control volumes a grid-cell average value is more representative of the values near the extrema at the element boundary than the quadrature

¹⁶⁰ point value. The relationship between the nodal values, the basis functions and the proposed
¹⁶¹ control volumes is illustrated schematically in one-dimension in parts (f) and (i) in Figure 2.

¹⁶² 3. Methods

¹⁶³ Here we focus on CAM-SE, however, in principle the methods apply to any element-based high-
¹⁶⁴ order Galerkin model. The physics grid in CAM-SE is defined by sub-dividing each element using
¹⁶⁵ equi-angular gnomonic coordinate lines to define the sides of the physics grid control volumes (see
¹⁶⁶ the Appendix for details). Note that the element boundaries are defined by equi-angular gnomonic
¹⁶⁷ grid lines. The notation $pg = 3$ refers to the configuration where the elements are divided into
¹⁶⁸ $pg \times pg = 3 \times 3$ equi-angular physics grid cells (see Figure 5) **resulting in a quasi-equal spherical**
¹⁶⁹ **area grid resembling the cubed-sphere.** Defining the physics grid by sub-dividing elements makes
¹⁷⁰ it possible to use the same element infrastructure as already used in CAM-SE, thereby facilitating
¹⁷¹ its implementation. Here we make use of the $ne30np4$ and $ne30pg3$ grids that use GLL quadrature
¹⁷² point physics grid (physics and dynamics grid coincide), and the same ($pg = 3$) resolution quasi
¹⁷³ equal-area physics grids, respectively. In all configurations we use degree three Lagrange basis
¹⁷⁴ ($np = 4$) and $ne \times ne = 30 \times 30$ elements on each cubed-sphere panel.

¹⁷⁵ A consequence of separating physics and dynamics grids is that the atmospheric state must be
¹⁷⁶ mapped to the physics grid and the physics tendencies must be mapped back to the dynamics
¹⁷⁷ grid. This is discussed in separate sections below. When separating physics and dynamics grids
¹⁷⁸ it is advantageous to use a vertical coordinate that is static during physics-dynamics coupling.
¹⁷⁹ This was one motivation to switch to a dry-mass vertical coordinate in CAM-SE (?); since dry
¹⁸⁰ mass remains constant throughout physics the dry-mass vertical coordinate remains fixed during
¹⁸¹ physics-dynamics coupling. **The dry mass coordinate subsequently evolves as floating Lagrangian**

182 layers by the dynamics (?) periodically mapped back to a reference hybrid-sigma-pressure coor-
183 dinate after ?. All variables mapped between grids are collocated, layer-mean values (?).

184 *a. Mapping state from dynamics grid (GLL) to physics grid (pg)*

185 The dynamics state is defined on the GLL grid in terms of temperature $T^{(gll)}$, zonal wind com-
186 ponent $u^{(gll)}$, meridional wind component $v^{(gll)}$, and dry pressure level thickness $\Delta p^{(gll)}$. In the
187 mapping of the atmospheric state to the physics grid it is important that the following properties
188 are met:

- 189 1. conservation of scalar quantities such as mass and dry thermal energy,
- 190 2. for tracers; shape-preservation (monotonicity), i.e., the mapping method must not introduce
191 new extrema in the interpolated field, in particular, negatives,
- 192 3. consistency, i.e., the mapping preserves a constant,
- 193 4. linear correlation preservation.

194 Other properties that may be important, but not pursued here, includes total energy conservation
195 and axial angular momentum conservation. Total energy is a quadratic quantity that is inherently
196 difficult to conserve unless one maps total energy requiring one to diagnose either temperature or
197 momentum components. For example, enforcing total energy conservation locally using, e.g., ?'s
198 method where total energy and velocity components are remapped and temperature is a derived
199 variable, has proven problematic (C. Chen, personal communication). Similarly conservation of
200 axial angular momentum is problematic. Conservation of angular momentum requires one to
201 interpolate the zonal and meridional components of momentum which creates large errors near
202 the poles. To avoid the pole problem we interpolate contra-variant components of the momentum
203 vector, which violates axial angular momentum conservation.

204 We argue that the most consistent method for mapping scalar state variables from the GLL grid
 205 to the physics grid is to integrate the Lagrange basis function representation (used by the SE dy-
 206 namical core) over the physics grid control volumes, i.e., integrate the basis function representation
 207 of $\Delta p^{(gll)} \times T^{(gll)}$ and $\Delta p^{(gll)}$ over the physics grid control volume (see, e.g., ??)

$$\Delta p^{(pg)} = \frac{1}{A^{(pg)}} \int_{A^{(pg)}} \Delta p^{(gll)} dA, \quad (1)$$

$$T^{(pg)} = \frac{1}{A^{(pg)} \Delta p^{(pg)}} \int_{A^{(pg)}} T^{(gll)} \Delta p^{(gll)} dA, \quad (2)$$

208 where $A^{(pg)}$ is the physics grid area. The integrals are numerically computed using the GLL
 209 quadrature rule **on each physics grid element, which exactly (to machine precision) integrates the**
 210 **basis functions over the pg control volumes (?)**. Thermal energy and dry air mass is conserved
 211 and the mapping is consistent. For the wind, which is a vector, the zonal and meridional wind
 212 components are mapped by transforming to contra-variant wind components, evaluating the basis
 213 function representation thereof at the equi-angular center of the physics grid control volumes and
 214 then transformed back to latitude-longitude coordinate system winds. All of the operations are
 215 local to the element and do not require communication between elements.

216 The mapping of tracers is more problematic since the SE basis function representation is os-
 217 cillatory although the shape-preserving filter guarantees shape-preservation at the GLL nodes
 218 (?). To avoid this issue we use the CAM-SE-CSLAM version of CAM-SE (Conservative Semi-
 219 Lagrangian Multi-tracer transport scheme ?), where tracers are advected on the $pg = 3$ physics
 220 grid **using the inherently mass and linear-correlation preserving CSLAM algorithm**. Note that in
 221 CAM-SE-CSLAM the dry mass internally predicted by CSLAM, $\Delta p^{(cslam)}$, is, by design, equal
 222 to $\Delta p^{(gll)}$ integrated over the CSLAM/physics grid control volume (?). Since the tracer grid and
 223 physics grids are co-located and $\Delta p^{(pg)} = \Delta p^{(cslam)}$ then the mass conservation, correlation preser-
 224 vation, consistency and shape-preservation constraints are inherently fulfilled.

225 b. *Mapping tendencies from physics grid (pg) to dynamics grid (GLL)*

226 The physics tendencies are computed on the finite-volume physics grid and are denoted
227 $f_T^{(pg)}$, $f_u^{(pg)}$, $f_v^{(pg)}$, and $f_m^{(pg)}$. Note that dry air mass is not modified by physics and hence there
228 is no tendency for dry mass, $f_{\Delta p} \equiv 0$. Also, it is important to map tendencies and not state from
229 the physics grid to GLL grid otherwise one will get spurious tendencies from mapping errors when
230 the actual physics tendency is zero (unless a reversible map is used).

231 It is important that this process:

232 1. for tracers; mass tendency is conserved,

233 2. for tracers; in each tracer grid cell the mass tendency from physics must not exceed tracer
234 mass available in tracer grid cell (it is assumed that the physics tendency will not drive tracer
235 mixing ratio negative on the physics grid),

236 3. linear correlation preservation,

237 4. consistency, i.e., the mapping preserves a constant tendency.

238 Other properties that may be important, but not pursued here, includes total energy conservation
239 (incl. components of total energy) and axial angular momentum conservation. Scalar variables
240 are mapped from the physics grid to GLL grid using a tensor-product Lagrange interpolation in
241 two dimensions (i.e., we assume that the pressure variations in the vertical are small). The local
242 coordinates on a cubed-sphere are discontinuous at the element edges so the interpolation requires
243 special attention at the cube corners and edges. The details are provided in the Appendix. Lagrange
244 interpolation preserves a constant (including zero) and linear correlations. Tracer and physics grids
245 are co-located so tracer mass, tracer shape, and tracer correlations are trivially preserved on the
246 tracer grid; and the inconsistency in point 2 above will not appear.

247 Mapping from pg to GLL grids while conserving mass was found to be difficult without ex-
248 cessive grid imprinting at element edges. Mass-conservation (using conventional finite-volume
249 methods) requires a control volume to be defined around the GLL points (see Figure 4 in this
250 paper or Figure 8b in [?](#)). These volumes are artificial and not consistent with the SE method.
251 Integrating the CSLAM reconstruction of water tracers of such artificial control volumes led to
252 GLL node grid imprinting in the mapping and will not preserve a constant mixing ratio since the
253 mapping of $\Delta p^{(pg)}$ to GLL will not yield the GLL node value for dry pressure-level thickness (i.e.,
254 the maps are not reversible). A reversible map requires that the number of degrees of freedom on
255 the source mesh ($pg3$ has 9 degrees of freedom) equal the number of degrees of freedom on the
256 target mesh ($np4$ grid has 16 degrees of freedom). This condition is violated by construction for
257 individual elements.

258 It was also found important to use an interpolator that is smooth across element boundaries.
259 Using an algorithm that only uses information from an element of control volumes will (at best)
260 be C^0 at the element boundaries and therefore lead to boundary node grid imprinting. A stencil that
261 extends beyond one element is therefore necessary. After much experimentation, the best results
262 in terms of grid-imprinting were obtained with tensor-cubic interpolation (see the Appendix for
263 details) and by using the CAM-SE-CSLAM configuration (which requires the same boundary
264 exchange/communication as used in CSLAM).

265 c. *Time splitting and physics-dynamics coupling*

266 The physics and dynamics are integrated in time using a sequential-update approach (e.g., [?](#)).
267 The dynamical core is sub-cycled over the (usually) longer physics time-step, Δt_{phys} , e.g., the ver-
268 tical remapping time-step Δt_{remap} is cycled $rsplit$ times, totaling to Δt_{phys} . In CAM-SE, a fraction
269 of the physics forcing, e.g., $f_q \times \Delta t_{remap}$ is applied at the beginning of each $rsplit$ vertical remap

270 subcycles, such that the full forcing ($f_q \times \Delta t_{phys}$) is realized over the course of a physics time-step.
271 This approach of dribbling the tendencies over sub-intervals has the advantage of reducing grav-
272 ity wave noise (?), but may disrupt tracer mass conservation (?). In CAM-SE-CSLAM, all but
273 the tracer mass quantities are dribbled, with tracer mass receiving the full physics update, e.g.,
274 $f_q \times \Delta t_{phys}$, applied only at the beginning of the first remap sub-cycle, and thereby conserving
275 tracer mass. This is the *ftype* = 2 configuration described in detail in Section 3.6.3 in ?.

276 In the SE integration of the equations of motion on the GLL grid the water species are
277 needed in the computation of the pressure gradient force and generalized expressions for heat
278 capacity at constant pressure c_p , etc. Hence the mixing ratios for water vapor and dynami-
279 cally/thermodynamically active condensates (e.g., cloud liquid and cloud ice) are needed on the
280 GLL grid. We have chosen to advect the water species on the GLL grid using the SE method as
281 well as on the physics grid using CSLAM. Every time physics updates the water species on the
282 CSLAM grid, a forcing term (equal to the difference between updated CSLAM water variables and
283 the SE values) is applied to the GLL water variables using dribbling so that the CSLAM solution
284 and SE solution for water species are tightly coupled.

285 4. Results

286 A hierarchy of idealized model configurations are presented in order to elucidate the differ-
287 ences between CAM-SE and CAM-SE-CSLAM (available from the CESM2.1 release; <https://doi.org/10.5065/D67H1H0V>). Here, the configurations are presented in order of increasing
288 complexity, each with a pair of approximately 1° simulations, pertaining to the *ne30np4* (CAM-
289 SE) and *ne30pg3* (CAM-SE-CSLAM) grids, and a $\Delta t_{phys} = 1800$ s.
290

291 a. *Moist Baroclinic Wave*

292 The moist baroclinic wave test case was developed as part of the ‘CESM Simple Models’ project
293 (??), and included in the release of CESM2. It is effectively the dry test-case of ??, but initialized
294 with moisture and coupled to the Kessler moist physics routine (??). For more details on this
295 test case (which was part of the 2016 Dynamical Core Model Intercomparison Project, ??), see
296 Section 4.1 in ?. A measure of the uncertainty in the reference solution, the L_2 difference norm
297 between two high-resolution solutions using different dynamical cores, was also presented in ?
298 and provided again here in Figure 6. The L_2 norm between CAM-SE and CAM-SE-CSLAM lies
299 below the uncertainty of the reference solution, indicating their differences are insignificant.

300 The flow field of the baroclinic wave test is used to drive the terminator “toy”-chemistry test of
301 ???. The terminator test is used to assess linear-correlation preservation using two reactive species
302 advected across the terminator line. The model is initialized with species for which their weighted
303 sum, Cl_y , is a constant (constant surface pressure and constant mixing ratio; $Cl_y = Cl + 2Cl_2 =$
304 $4 \times 10^{-6} \text{ kg/kg}$), such that if tracer correlations are preserved, then the column-integrated weighted
305 sum of the species should not vary in time. Figure 7 provides a snapshot of the vertically integrated
306 weighted sum of species at day 15. In CAM-SE, the tracer correlations are not preserved at
307 day 15 and the field is populated by overshoots and undershoots. In contrast, by day 15, CAM-
308 SE-CSLAM still conserves tracer correlations to within machine precision, consistent with the
309 previous results of this test-case initialized with a dry baroclinic wave (??).

310 *b. Aqua-planets*

311 Two year long aqua-planet simulations are performed using CAM-SE and CAM-SE-CSLAM,
312 using the CAM4 physics package (??), as discussed in Section 2. Away from the grid-scale, the
313 mean states in the two models are very similar. Figure 8 shows the zonal-mean climatological
314 precipitation rates in CAM-SE and CAM-SE-CSLAM. Considering how sensitive this aqua-planet

315 configuration is to design choices in CAM-SE (?), it is somewhat unexpected that the zonal means
316 look so similar to one another.

317 A plot similar to Figure 3a is constructed for the CAM-SE-CSLAM simulation, a probability
318 density distribution of upward ω conditionally sampled based on location within the element. Like
319 Figure 3a, Figure 3b divides up the control volumes by corner, edge and interior cells. Through the
320 use of the quasi-equal area physics grid, the dynamical core state appears more or less independent
321 of location within the element, a marked improvement over CAM-SE. Since the state is approxi-
322 mately independent of in-element location, it follows that the physics forcing, which is evaluated
323 from the dynamical core state, may be expected to also show an improvement in grid-imprinting.

324 The low-level, mean and variance of the temperature tendencies from the physics, on the GLL
325 grid, $f_T^{(gll)}$, in the two simulations are shown in Figure 9. The mean states in the two models
326 resemble one another, consistent with the zonal mean precipitation rates (Figure 8). The mean
327 physics tendencies contains modest grid imprinting in CAM-SE (barely visible near the storm-
328 track regions), while in the variance field, grid imprinting is both ubiquitous and unmistakable.
329 The variance is larger on boundary nodes, manifesting as a ‘stitching’ pattern resembling the
330 cube-sphere grid. In CAM-SE-CSLAM, the grid imprinting is all but eliminated based on the
331 mean and variance of the physics tendencies (Figure 9), consistent with our expectation.

332 As stated in Section 3, the mapping of the state to the physics grid and the reverse interpolation
333 of physics tendencies to the GLL grid is not total energy conserving. CAM has a global energy
334 fixer (?) which can be used to estimate the errors associated with the mapping algorithms. To do
335 so, it is presumed that there are no compensating mapping errors in going to and from the physics
336 and dynamics grids, and that CAM-SE-CSLAM and CAM-SE have the same energy dissipation
337 rates. Under these assumptions the spurious globally integrated total energy errors due to the

338 mapping algorithm is estimated to be approximately 0.0025 W/m^2 in the aqua-planet simulations.
339 In comparison, the dynamical core total energy dissipation is on the order of 0.1 W/m^2 (?).

340 *c. Held-Suarez with Topography*

341 Grid imprinting associated with the flow around obstacles is more problematic than that en-
342 countered on the aqua-planets. In order to diagnose grid imprinting due to topographic flow, an
343 idealized Held-Suarez configuration (?) is outfitted with real world topography after ??, and run
344 for two years. Figure 10 shows the mean ω at two different vertical levels in the middle tropo-
345 sphere. **The data are presented as a raster plot on their respective unstructured grids, in order to**
346 **delineate whether a particular value is associated with an interior, edge or element boundary node.**

347 At higher latitudes (e.g., the southern Andes), the flow is smooth, conforming reasonably to the
348 underlying topography. At lower latitudes (within 20 to 30 degrees from the equator), over the
349 Andes or the Himalayas, there is a clear preference for extrema to occur at the element bound-
350 aries (Figure 10). The vertical structure of ω in regions of strong grid-imprinting indicates full-
351 troposphere upward/downward motion (not shown). Grid imprinting is therefore more common
352 in regions of weak stratification, such as occurs in the deep tropics, with forced up-slope flow
353 facilitating the release of gravitational instability. Resolved updrafts/downdrafts often align with
354 the element boundaries due to its systematically tighter pressure gradients.

355 Through the use of the quasi-equal area physics grid, grid imprinting due to topographic flow is
356 reduced (Figures 10). Figure 10 also shows the state in CAM-SE-CSLAM, but on the GLL grid.
357 Arguably, grid imprinting due to topography in CAM-SE-CSLAM is not much of an improvement
358 over CAM-SE, viewed from the GLL grid. The native topography lives on the physics grid, and the
359 topography is mapped to the nodal points at run-time in CAM-SE-CSLAM. Mapping topography
360 to the quadrature nodes ensures that no new extrema will be introduced to the boundary nodes,

361 where the solution is least smooth. This effect can not be very large, since the grid noise is similar
362 in CAM-SE and CAM-SE-CSLAM on the GLL grid. From the perspective of the physics grid,
363 the CAM-SE-CSLAM solution clearly mitigates the influence of grid-induced extrema on the state
364 (Figure 10). The reduction in grid imprinting in CAM-SE-CSLAM is therefore almost entirely a
365 result of the smoothing effect of integrating the basis functions over the control volumes of the
366 physics grid.

367 *d. AMIP type simulations*

368 A pair of 20 year-long AMIP type simulations are performed, using CAM, version 6 physics
369 package (CAM6) and using perpetual year 2000 SST boundary conditions (*F2000climo* compset
370 in CESM2.0; <https://doi.org/10.5065/D67H1H0V>). Figure 11 shows the climatological pre-
371 cipitation fields in CAM-SE (left) and CAM-SE-CSLAM (middle), and over the same mountain-
372 ous regions as in Figure 10. The plots have some similar features to the ω field in the Held-Suarez
373 runs; the greater variance at lower latitudes, and on the windward side of the mountains are broadly
374 similar. CAM-SE-CSLAM has a lower spatial variance, e.g., the lack of extrema over the Andes
375 at about 15° S compared to CAM-SE, and the grid-scale precipitation peak over the Himalayas
376 at about 30° N. The difference plot (Figure 11; right panel) is more broadly populated by blue,
377 purple and white contours, indicating that CAM-SE has, in general, larger magnitude precipitation
378 rates over high topography. The difference plots also highlight a couple of zonally aligned strips
379 of anomalous precipitation, in particular, near the foot of the Himalayas in CAM-SE. These bands
380 are in the same location as the bands of precipitation identified in CAM-SE in ? (their Figure 7),
381 but using CAM, version 5 physics, of which they argue are spurious in nature.

382 To assist in identifying whether a particular precipitation pattern is spurious, an *F2000climo*
383 simulation is carried out using the finite-volume dynamical core that uses a regular latitude-

longitude $0.9^\circ \times 1.25^\circ$ grid (CAM-FV; $f09$ grid; ?). CAM-FV is the default low resolution model in CESM2.0, and with its smoothly varying grid, does not suffer from the Quadrature Node Problem (Section 2). Figure 12 shows the global precipitation fields in CAM-SE, CAM-SE-CSLAM and CAM-FV, compared to an observational dataset, the Global Precipitation Climatology Project (GPCP; 1979-2003) gridded dataset (?). The magnitude of the precipitation rates in all three models are higher than the GPCP dataset, primarily over land in the Tropics (note the lack of red contours in the GPCP dataset), which should be interpreted cautiously due to widely-accepted issues in constructing a reliable, gridded, global precipitation dataset. At lower latitudes, CAM-FV has lower spatial variance, and overall lower magnitudes, compared with CAM-SE. The GPCP dataset indicates that perhaps the precipitation rates in low-latitude mountainous regions in CAM-FV and CAM-SE are larger than in reality. Following suit, the reduction in magnitude and spatial variance in precipitation in these regions in CAM-SE-CSLAM may be interpreted as an improvement over CAM-SE.

5. Conclusions

Element-based high-order Galerkin Methods possess many of the attractive qualities recommended for next generation global atmospheric models. Among these, high-order accuracy is achieved with minimal communication between elements, allowing for near perfect scaling on massively parallel systems. Element communication amounts to a numerical flux applied to the element boundaries, reconciling overlapping solutions of adjacent elements but degrading the smoothness of the boundary nodes in the process (to C^0). For non-smooth problems, gradients are systematically tighter at the element boundaries, and local extrema often characterize the boundary nodes. This behavior is illustrated using NCAR's Community Atmosphere Model with Spectral

406 Elements dynamics (CAM-SE) in an aqua-planet configuration, in a Held-Suarez configuration
407 with real-world topography **and in an AMIP type configuration.**

408 The authors argue that the conventional physics-dynamics coupling paradigm, in which the
409 physical parameterizations are evaluated on the dynamical core grid, exacerbates grid imprinting.

410 A separate physics grid is proposed and implemented in CAM-SE, and referred to as CAM-SE-
411 CSLAM, through dividing the elements into quasi-equal areas with equivalent degrees of freedom.

412 The state is mapped to the physics grid with high-order accuracy through integrating CAM-SE's
413 Lagrange basis functions over the control volumes. Control volumes near element boundaries now

414 represent a state in the vicinity of the extrema produced through the boundary exchange, as op-
415 posed to the the nodal value itself. These control volumes are also compatible with a 'large-scale

416 state' as required by the physical parameterizations. The physical parameterizations are evalu-
417 ated on the finite volume grid, and the forcing terms are mapped back to the dynamical core grid

418 using a cubic tensor-product Lagrange interpolation. In aqua-planet simulations, evaluating the
419 parameterizations on the physics grid removes any obvious dependence of proximity to the ele-

420 ment boundary, resulting in a more realistic state with negligible grid imprinting. The mapping
421 algorithm does not conserve total energy, but it is estimated that these errors are one to two orders

422 of magnitude less than the total energy dissipation from the dynamical core.

423 In CAM-SE-CSLAM, the physics grid replaces the default CAM-SE quadrature point-based
424 coupler grid (Figure 4) to compute fluxes between model components in the Community Earth

425 System Model (CESM). The appeal here is two-fold. Through integrating the Lagrange basis
426 functions over control volumes, one can be certain that the fluxes computed from this grid are a

427 volume averaged flux. **The same can not be said for CAM-SE, where artificial control volumes**
428 **(with sizes proportional quadrature weights) are constructed around nodal values and assumed to**

429 **represent the volume averaged state.** The second advantage of the new coupler grid is that extrema

430 occurring on boundary nodes may no longer influence other model components in simulations
431 without rough topography. While grid imprinting is effectively eliminated in the aqua-planets,
432 experiments with real-world topography (Held-Suarez and AMIP type configurations) reduces,
433 but does not entirely eliminate, imprinting from the mean state. The quasi-equal area physics grid
434 is nonetheless effective at mitigating numerical nuances associated with high-order element-based
435 Galerkin methods, for non-smooth problems.

436 Future work will focus on the impact of using a coarser, $pg \times pg = 2 \times 2$ physics grid configu-
437 ration. The coarser physics grid may be more effective at reducing spurious noise over regions of
438 rough topography, while potentially reducing the computational overhead. Any advantages of us-
439 ing a coarser resolution physics grid will be weighed against any potential reduction in a model's
440 effective resolution.

441 *Acknowledgments.* NCAR is sponsored by the National Science Foundation (NSF). We thank
442 three anonymous reviewers for their helpful comments that significantly improved the clarity of
443 the manuscript. Herrington thanks NCAR's Computational and Information Systems Laboratory
444 (CISL) and NCAR's Climate and Global Dynamics division (CGD) for computational resources
445 and technical support. Herrington, Reed, and Lauritzen are grateful to the NCAR Advanced Study
446 Program graduate visitor program for funding Herrington's 12-month visit. Goldhaber was par-
447 tially supported by the Accelerated Climate Modeling for Energy (ACME) project, and work pack-
448 age 12 – 015334 “Multiscale Methods for Accurate, Efficient, and the Accelerated Scale-Aware
449 Models, both funded through the U.S. Department of Energy Office of Biological and Environ-
450 mental Research. Goldhaber is also partially supported through NSF award AGS-1500187 “De-
451 velopment and Testing of a Global Quasi 3-D multi Modeling Framework.” Model source code is
452 officially released with CESM2.1 (<https://doi.org/10.5065/D67H1H0V>).

APPENDIX

454 The mapping of the physics tendencies from the physics grid to the GLL grid is done with
 455 tensor-cubic Lagrange interpolation. The elements of the cubed-sphere in SE are created
 456 from an equi-angular gnomonic projection. Consider one element $(\alpha, \beta) \in [\alpha_1^{(elem)}, \alpha_2^{(elem)}] \times$
 457 $[\beta_1^{(elem)}, \beta_2^{(elem)}]$, where (α, β) are central angle coordinates and $\alpha_1^{(elem)}$ and $\alpha_2^{(elem)}$ are the min-
 458 imum and maximum central angles in the α -coordinate direction, respectively, and similarly for
 459 β . Let $\Delta\alpha^{(elem)} = \alpha_2^{(elem)} - \alpha_1^{(elem)}$ and $\Delta\beta^{(elem)} = \beta_2^{(elem)} - \beta_1^{(elem)}$. The physics grid cell central
 460 angle centers are located at

$$(\alpha_i^{(pg)}, \beta_j^{(pg)}) = \left[\alpha_1^{(elem)} + \left(i - \frac{1}{2}\right) \Delta\alpha^{(pg)}, \beta_1^{(elem)} + \left(j - \frac{1}{2}\right) \Delta\beta^{(pg)} \right], \quad (\text{A1})$$

461 where $\Delta\alpha^{(pg)} = \Delta\beta^{(pg)} = \frac{\Delta\alpha^{(elem)}}{pg} = \frac{\Delta\beta^{(elem)}}{pg}$. The interpolation is performed in central-angle co-
 462 ordinates using tensor product cubic interpolation. For elements located on a cubed-sphere edge
 463 or corner the coordinate system for neighboring elements may be on a different panel. To take
 464 into account this coordinate change the central angle locations of physics grid cell centers located
 465 on other panels are transformed to the coordinate system of the panel the element in question is
 466 located on (the transformations are given in, e.g., ?). An illustration is given in Figure 13 for an
 467 element located in the lower left corner of a panel. The element in question is $(\xi, \chi) \in (-1, 1)^2$
 468 where, for simplicity, we have transformed the element coordinates into normalized coordinates
 469 $(\xi, \chi) = \left(\frac{2(\alpha^{(pg)} - \alpha_1^{(elem)})}{\Delta\alpha^{(elem)}} - 1, \frac{2(\beta^{(pg)} - \beta_1^{(elem)})}{\Delta\beta^{(elem)}} - 1 \right)$; also used internally in the SE dynamical core
 470 (see, e.g., section 3.3 in ?). The GLL points are located at $-1, -1/\sqrt{1}, 1/\sqrt{5}$, and 1 in each coor-
 471 dinate direction. Near the edges/corners of an element cubic extrapolation is used if the centered
 472 stencil expands beyond the panel.

473 **References**

474 LIST OF FIGURES

- 475 **Fig. 1.** Example of CAM-SE GLL quadrature grids, marked with red filled circles, (a & c) on the
 476 cubed-sphere and (b & d) in an element. (a)-(b) and (c)-(d) use 4×4 ($np = 4$) and 8×8
 477 ($np = 8$) GLL quadrature points in each element, respectively. (a) and (c) have the same
 478 average grid-spacing at the Equator (7.5°) which is obtained by using (a) 4×4 ($ne = 4$)
 479 and (b) 2×2 ($ne = 2$) elements on each cubed-sphere face/panel, respectively. The element
 480 boundaries are marked with thick light blue lines. The grid configurations shown on (a) and
 481 (c) are referred to as $ne4np4$ and $ne2np8$, respectively. 26
- 482 **Fig. 2.** A one-dimensional schematic showing the relationship between the basis functions, the
 483 quadrature nodes and the proposed physics grid, over the coarse of a time-step. The filled
 484 circles are the GLL quadrature points in each element, which are connected by a Lagrange
 485 polynomials basis (curves). (a) Smooth initial condition are (b) advanced by the dynamics
 486 one Runge-Kutta step (blue), and (c) shows the solution after applying the DSS operator.
 487 Applying (d) grid-scale forcing to an element boundary node, (e) the basis representation is
 488 clearly C^0 at the element boundary. In contrast, (d) applying grid-scale forcing to an interior
 489 node (e) results in a smooth, C^∞ continuous field. (f),(i) Vertical bars pertain to the values
 490 on the physics grid, found through integrating the basis functions over the control volumes. 27
- 491 **Fig. 3.** Probability density distribution of instantaneous upward ω in a pair of aqua-planet simu-
 492 lations using CAM4 physics. Figure is constructed from one year of six hourly data, at
 493 all vertical levels. (a) $ne30np4$ configuration conditionally sampled for interior, edge and
 494 corner node control volumes, and similarly (b) for the $ne30pg3$ configuration. Note the con-
 495 sistent larger magnitude ω for boundary nodes compared with interior nodes in (a), and
 496 that the bias is substantially reduced through mapping to a quasi-equal area physics grid. 28
- 497 **Fig. 4.** An example of control volumes constructed around GLL quadrature points ($ne4np4$) so that
 498 the spherical area of the control volumes exactly match the quadrature weight multiplied by
 499 the metric factor. 29
- 500 **Fig. 5.** A schematic illustration of an element, indicating the relationship between (left) the dy-
 501 namical core grid, and (right) the proposed quasi-equal area physics grid. The physics grid
 502 contains $pg \times pg = 3 \times 3$ grid cells in each element. 30
- 503 **Fig. 6.** L_2 difference norms of the surface pressure field, p_s , in the moist baroclinic wave simu-
 504 lations. L_2 values lying within the yellow region fall below the estimate of the uncertainty in
 505 the reference solution (black curve), computed as the difference norm between two approx-
 506 imately 0.25° resolution versions of CAM, the spectral-element and finite-volume (CAM-
 507 FV) dynamical cores. 31
- 508 **Fig. 7.** Results of the terminator “toy”-chemistry test. Snapshot of the total column integrated,
 509 weighted sum of the species, $\langle Cl_y \rangle = \langle Cl \rangle + \langle 2Cl_2 \rangle$, in kg/kg, at day 15 of the moist baro-
 510 clinic wave test. (Top) CAM-SE, (Bottom) CAM-SE-CSLAM. 32
- 511 **Fig. 8.** Climatological zonal-mean total precipitation rate in the aqua-planets, computed from a pair
 512 of year long simulations. 33
- 513 **Fig. 9.** Mean (left) and variance (right) of the low level temperature tendencies from the physical
 514 parameterizations on the GLL grid, with the $ne30np4$ configuration, (top row) and $ne30pg3$
 515 configuration (bottom row), in a pair of year-long aqua-planet simulations after ?. Grid
 516 imprinting is observed along the element boundaries in $ne30np4$, but is absent from the
 517 $ne30pg3$ simulation. 34

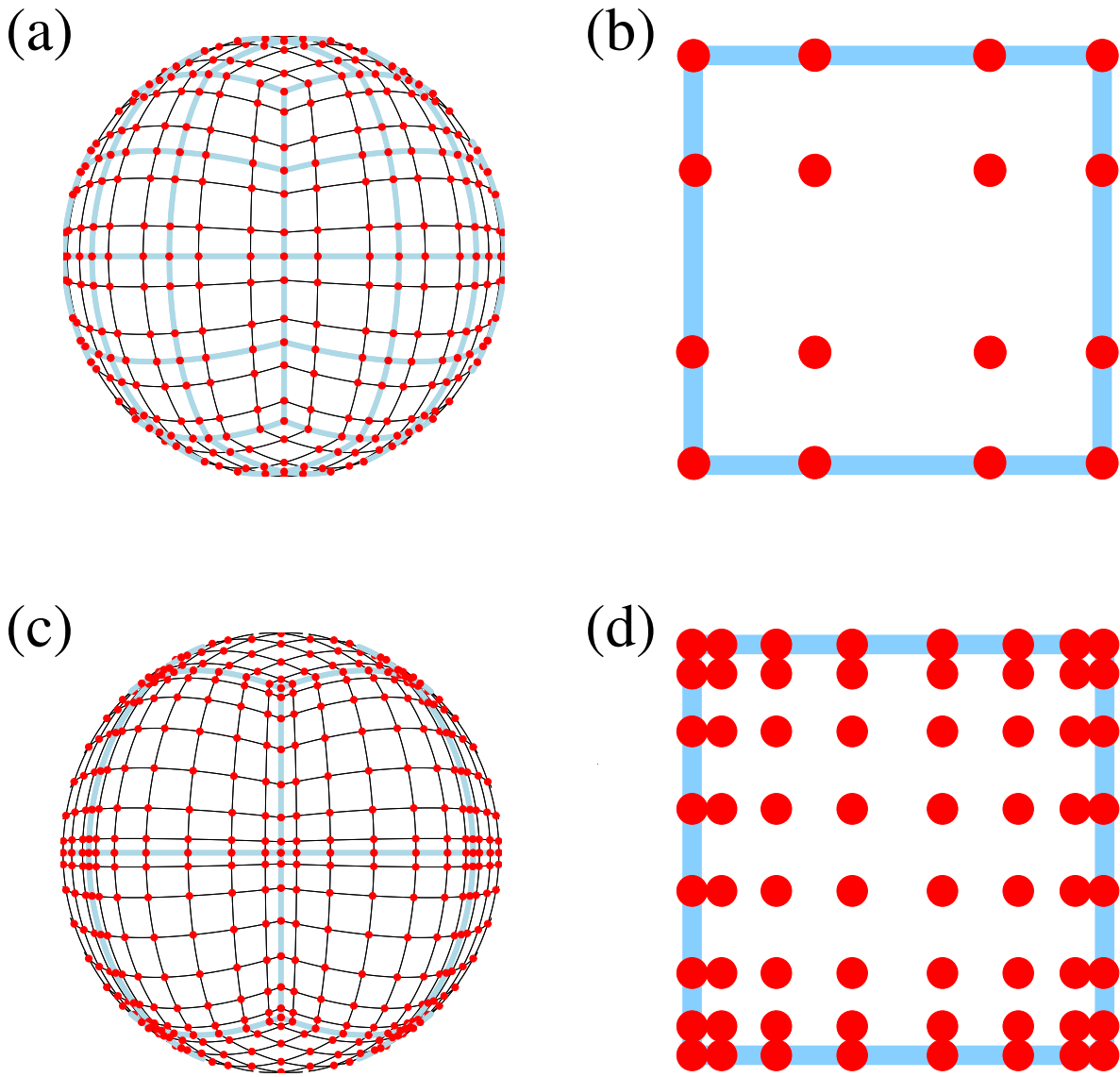
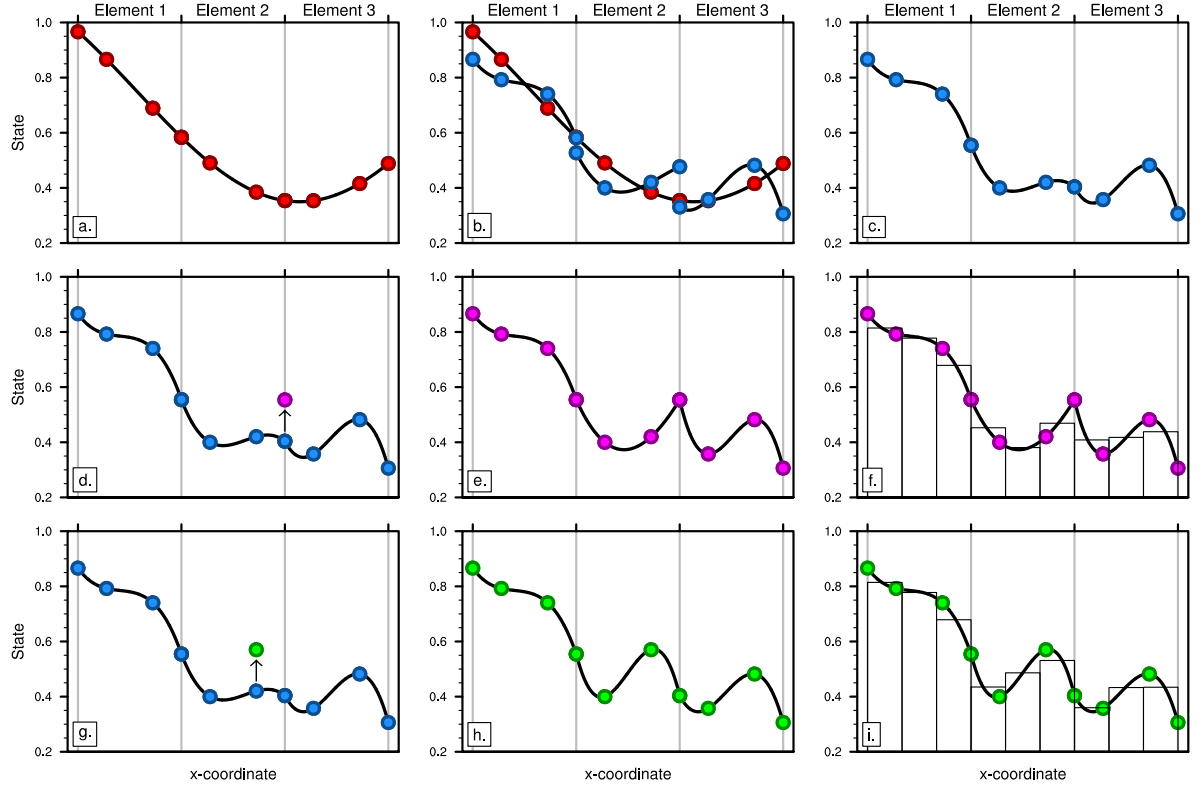


FIG. 1. Example of CAM-SE GLL quadrature grids, marked with red filled circles, (a & c) on the cubed-sphere and (b & d) in an element. (a)-(b) and (c)-(d) use 4×4 ($np = 4$) and 8×8 ($np = 8$) GLL quadrature points in each element, respectively. (a) and (c) have the same average grid-spacing at the Equator (7.5°) which is obtained by using (a) 4×4 ($ne = 4$) and (b) 2×2 ($ne = 2$) elements on each cubed-sphere face/panel, respectively. The element boundaries are marked with thick light blue lines. The grid configurations shown on (a) and (c) are referred to as $ne4np4$ and $ne2np8$, respectively.



547 FIG. 2. A one-dimensional schematic showing the relationship between the basis functions, the quadrature
 548 nodes and the proposed physics grid, over the coarse of a time-step. The filled circles are the GLL quadrature
 549 points in each element, which are connected by a Lagrange polynomials basis (curves). (a) Smooth initial con-
 550 dition are (b) advanced by the dynamics one Runge-Kutta step (blue), and (c) shows the solution after applying
 551 the DSS operator. Applying (d) grid-scale forcing to an element boundary node, (e) the basis representation is
 552 clearly C^0 at the element boundary. In contrast, (d) applying grid-scale forcing to an interior node (e) results
 553 in a smooth, C^∞ continuous field. (f),(i) Vertical bars pertain to the values on the physics grid, found through
 554 integrating the basis functions over the control volumes.

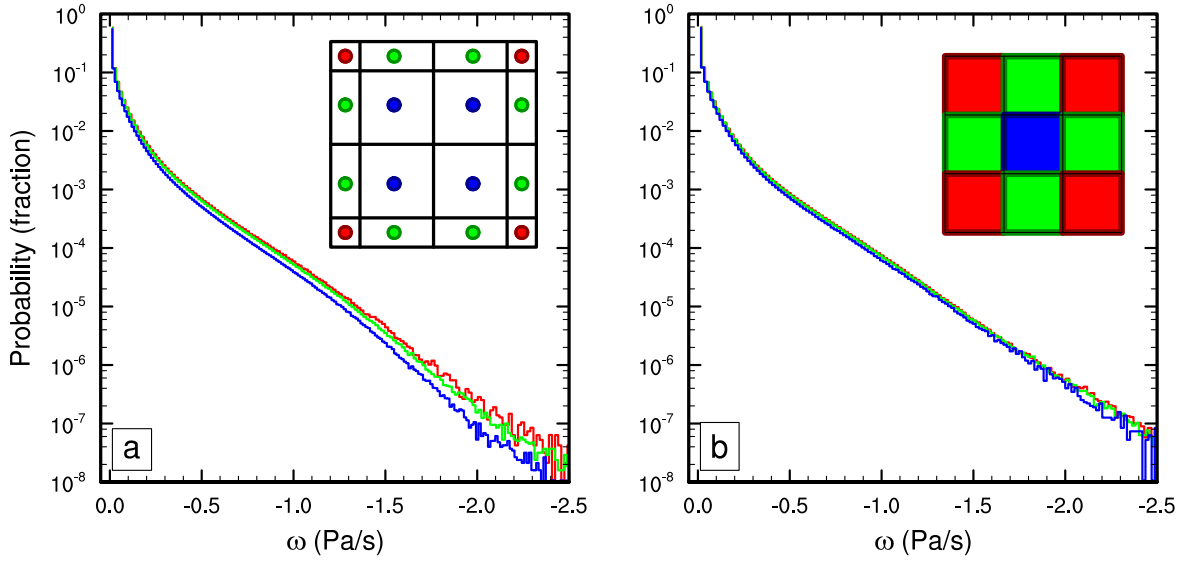
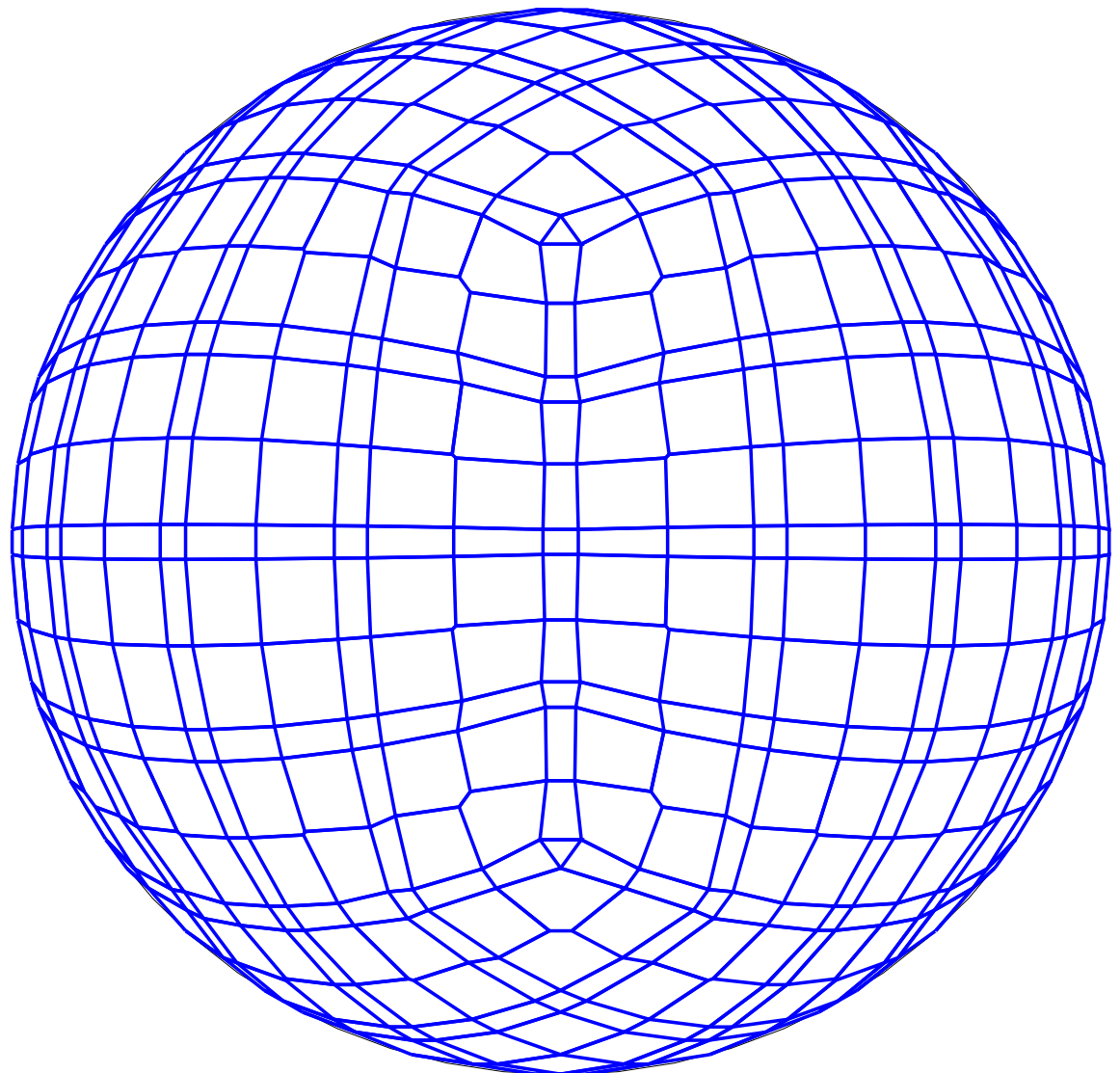
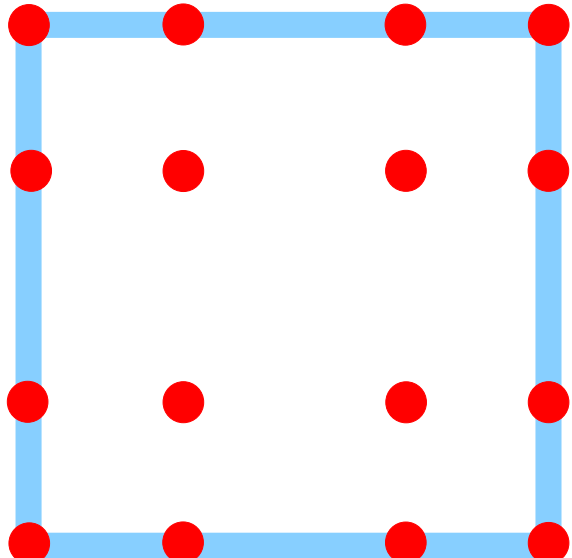


FIG. 3. Probability density distribution of instantaneous upward ω in a pair of aqua-planet simulations using CAM4 physics. Figure is constructed from one year of six hourly data, at all vertical levels. (a) *ne30np4* configuration conditionally sampled for interior, edge and corner node control volumes, and similarly (b) for the *ne30pg3* configuration. Note the consistently larger magnitude ω for boundary nodes compared with interior nodes in (a), and that the bias is substantially reduced through mapping to a quasi-equal area physics grid.

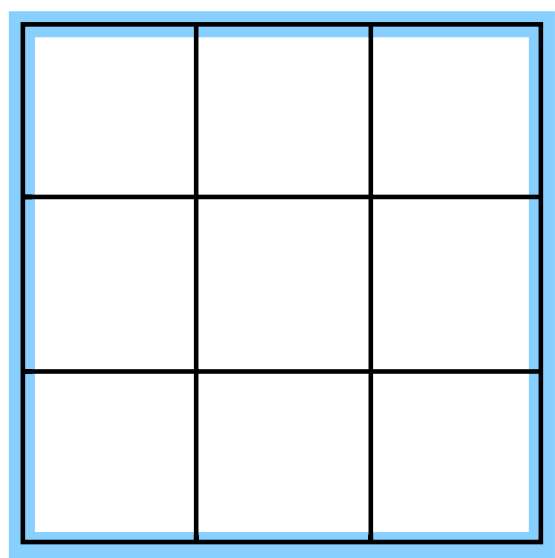


560 FIG. 4. An example of control volumes constructed around GLL quadrature points ($ne4np4$) so that the
561 spherical area of the control volumes exactly match the quadrature weight multiplied by the metric factor.

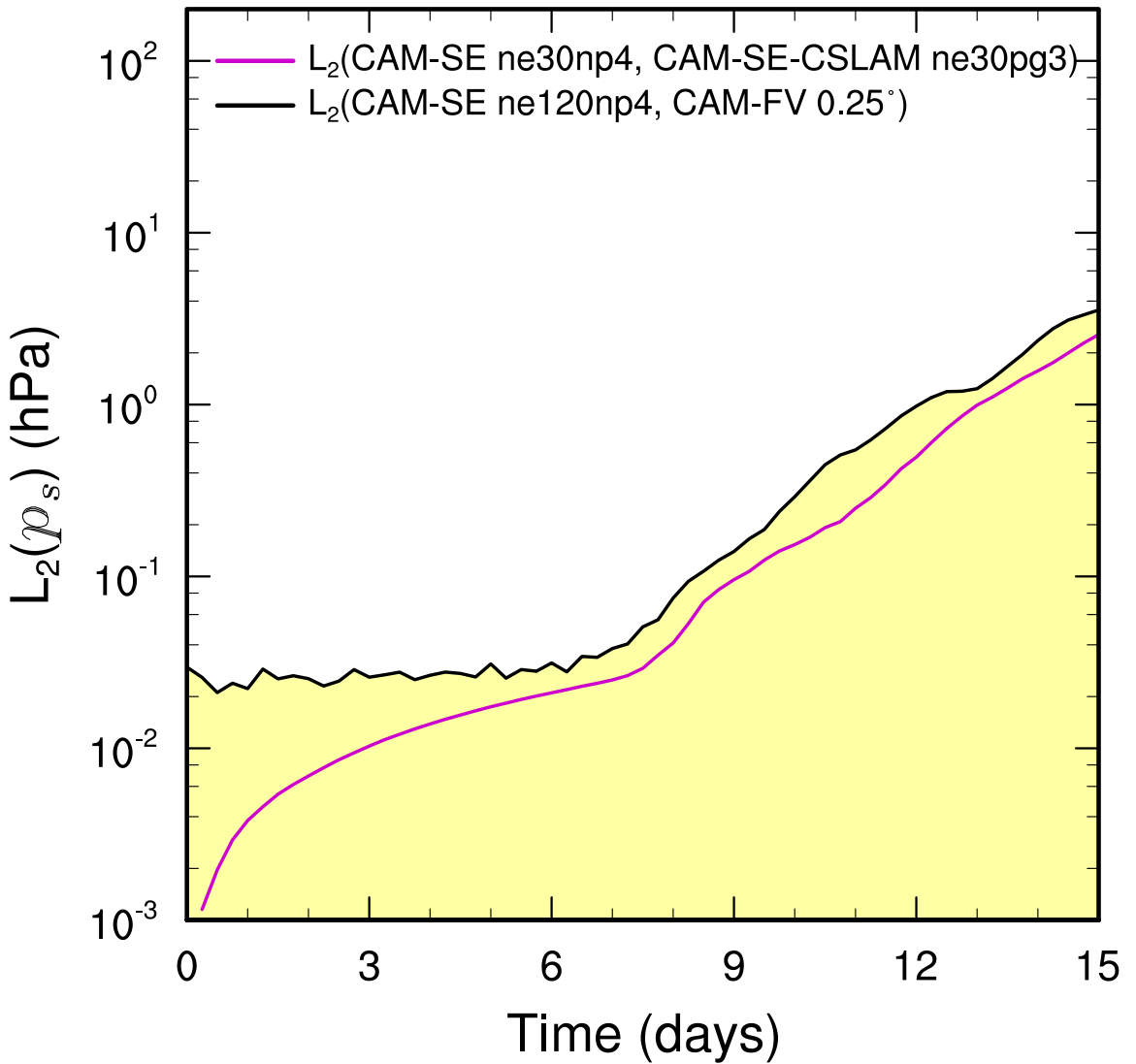
$np = 4$



$pg = 3$



562 FIG. 5. A schematic illustration of an element, indicating the relationship between (left) the dynamical core
563 grid, and (right) the proposed quasi-equal area physics grid. The physics grid contains $pg \times pg = 3 \times 3$ grid cells
564 in each element.



565 FIG. 6. L_2 difference norms of the surface pressure field, p_s , in the moist baroclinic wave simulations. L_2
 566 values lying within the yellow region fall below the estimate of the uncertainty in the reference solution (black
 567 curve), computed as the difference norm between two approximately 0.25° resolution versions of CAM, the
 568 spectral-element and finite-volume (CAM-FV) dynamical cores.

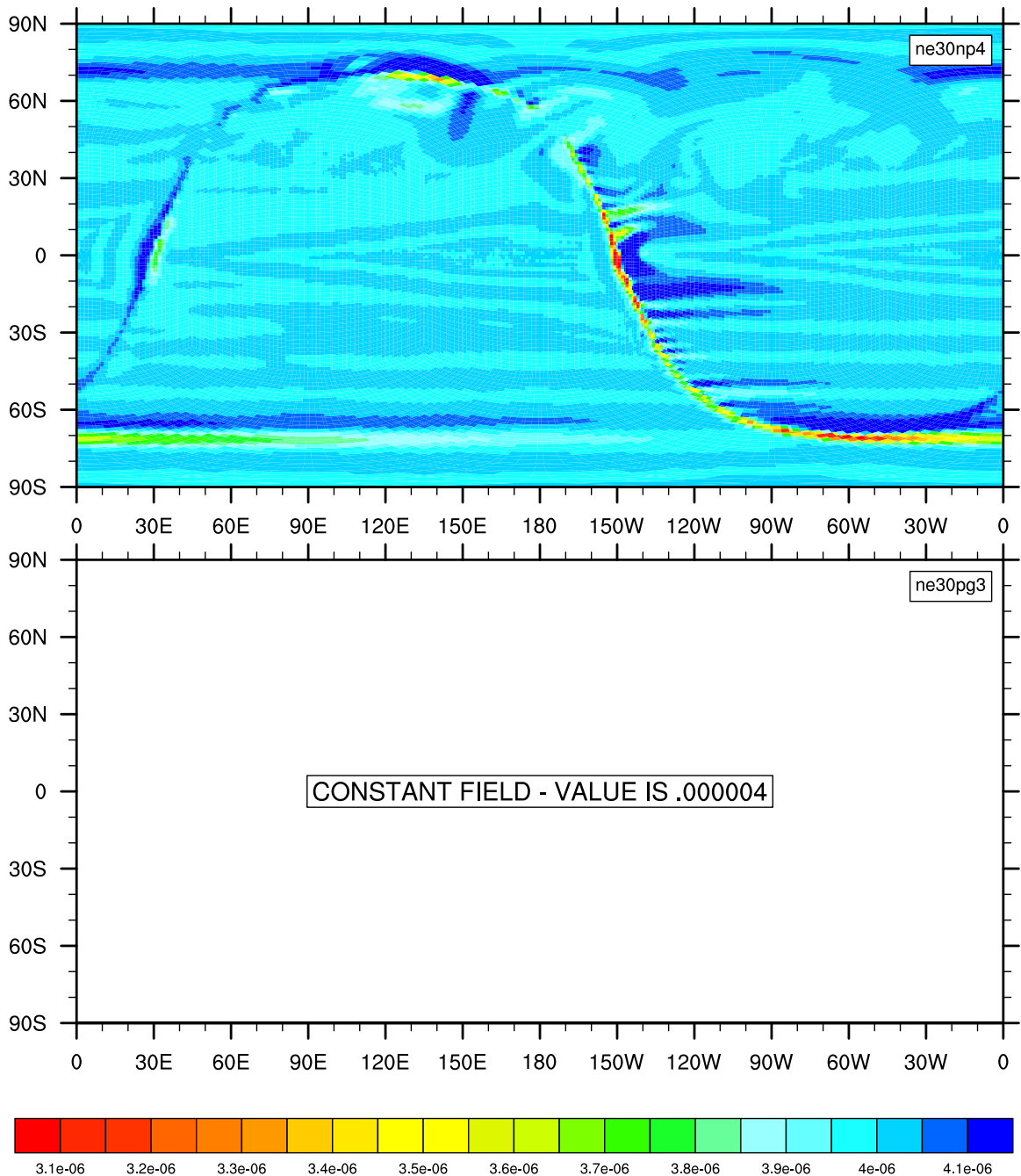
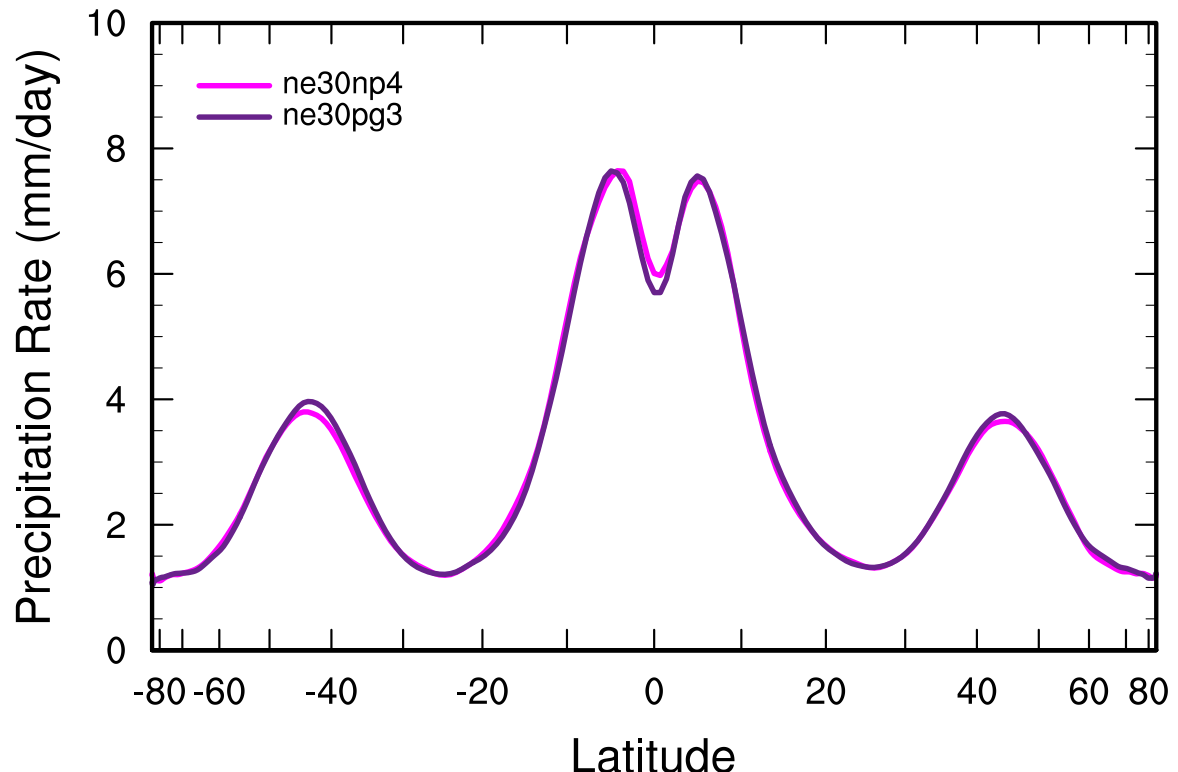
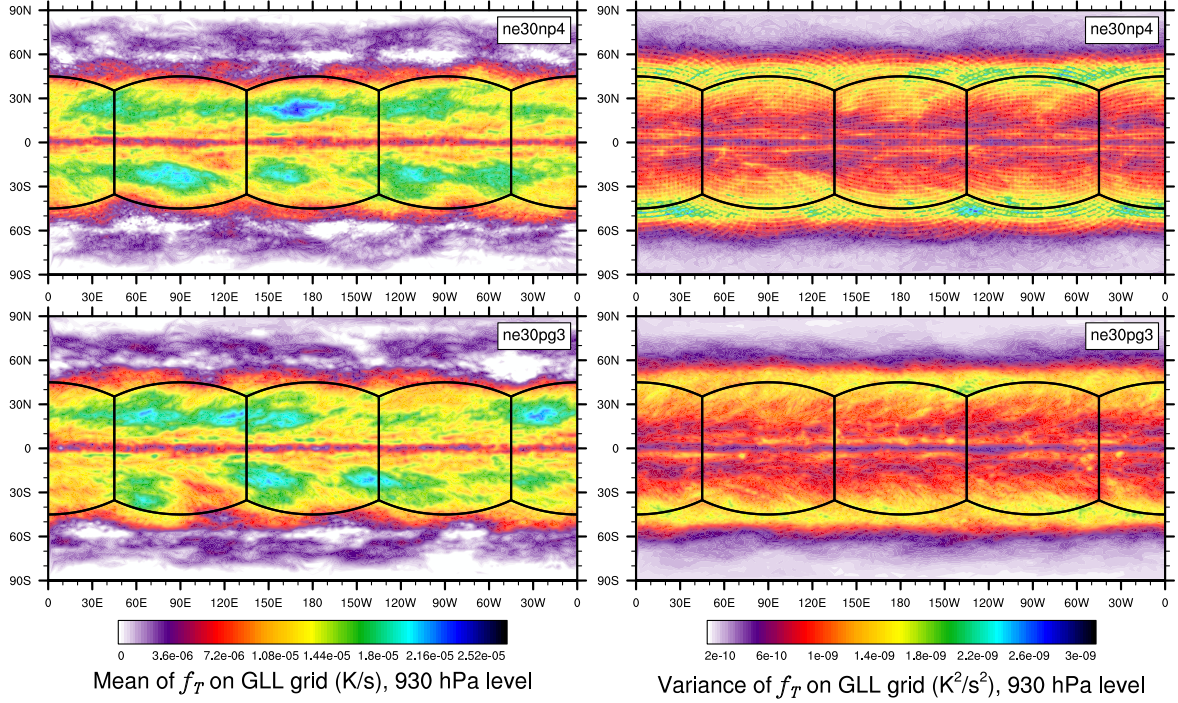


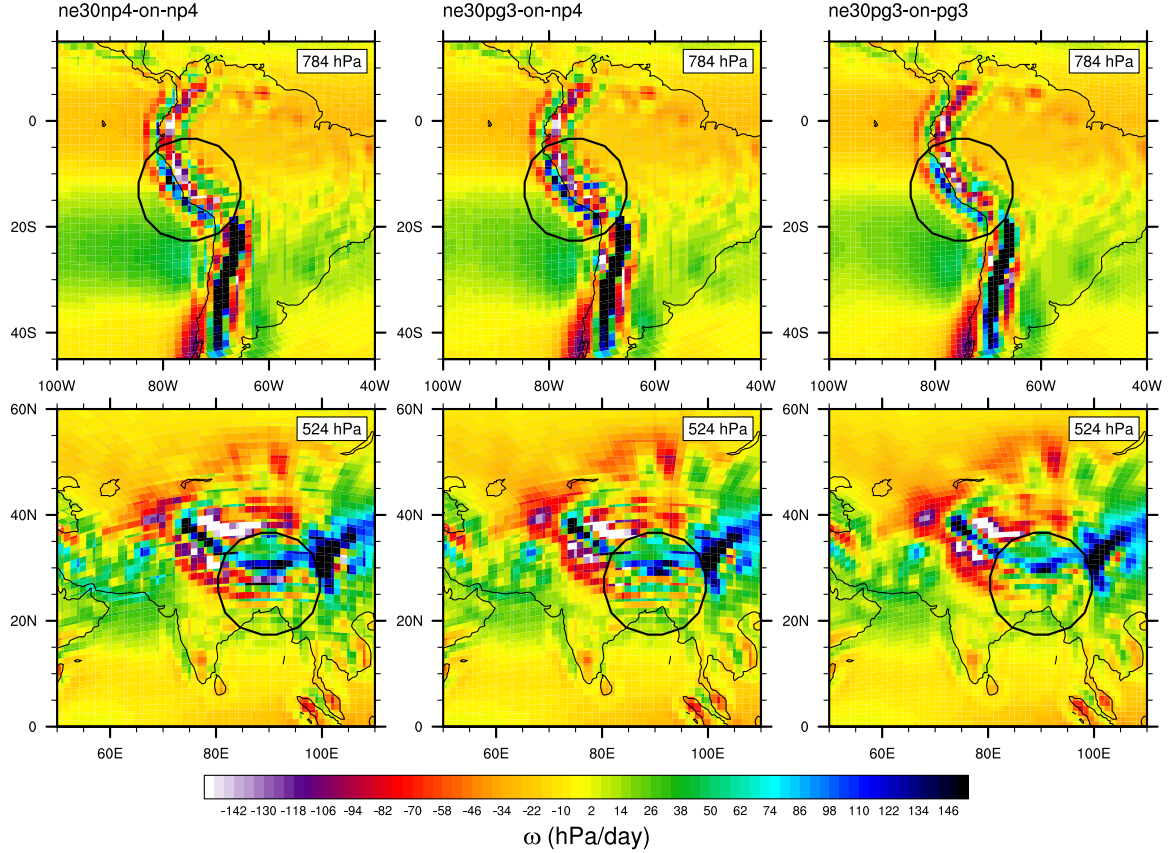
FIG. 7. Results of the terminator “toy”-chemistry test. Snapshot of the total column integrated, weighted sum
 $\langle Cl_y \rangle = \langle Cl \rangle + \langle 2Cl_2 \rangle$, in kg/kg, at day 15 of the moist baroclinic wave test. (Top) CAM-SE,
(Bottom) CAM-SE-CSLAM.



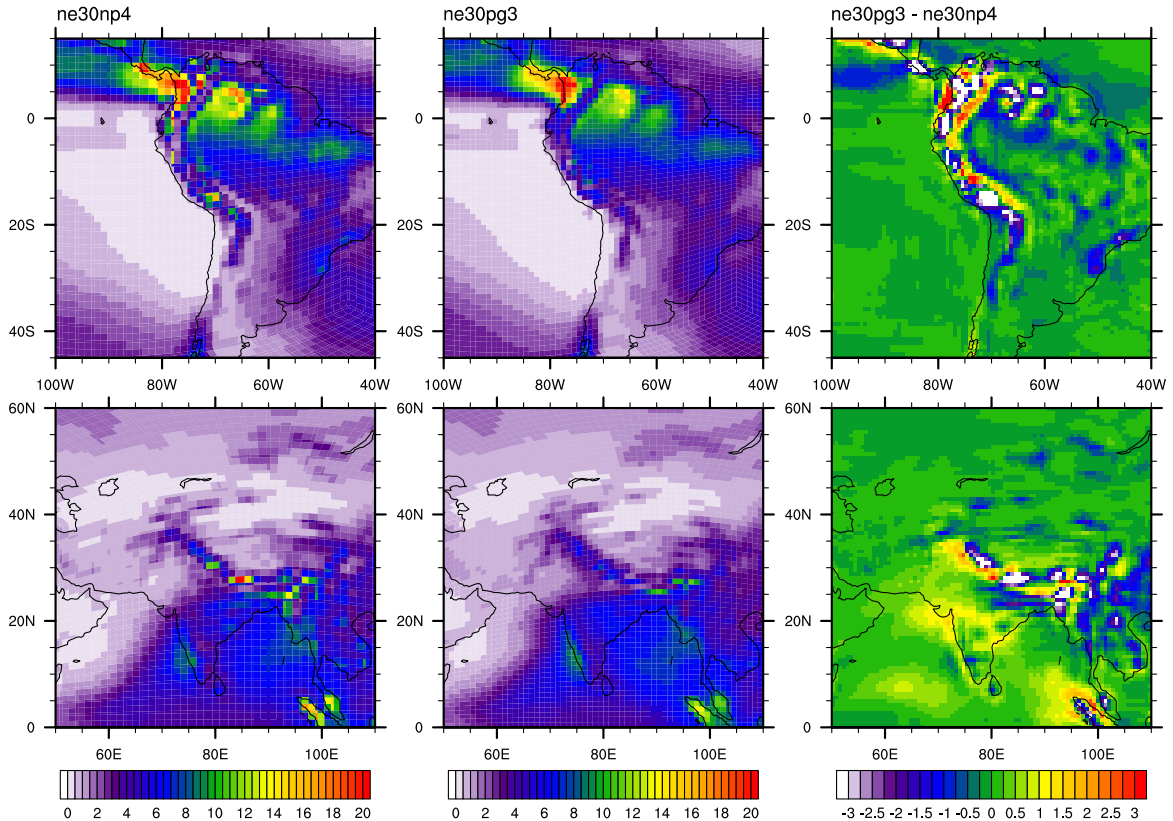
572 FIG. 8. Climatological zonal-mean total precipitation rate in the aqua-planets, computed from a pair of year
573 long simulations.



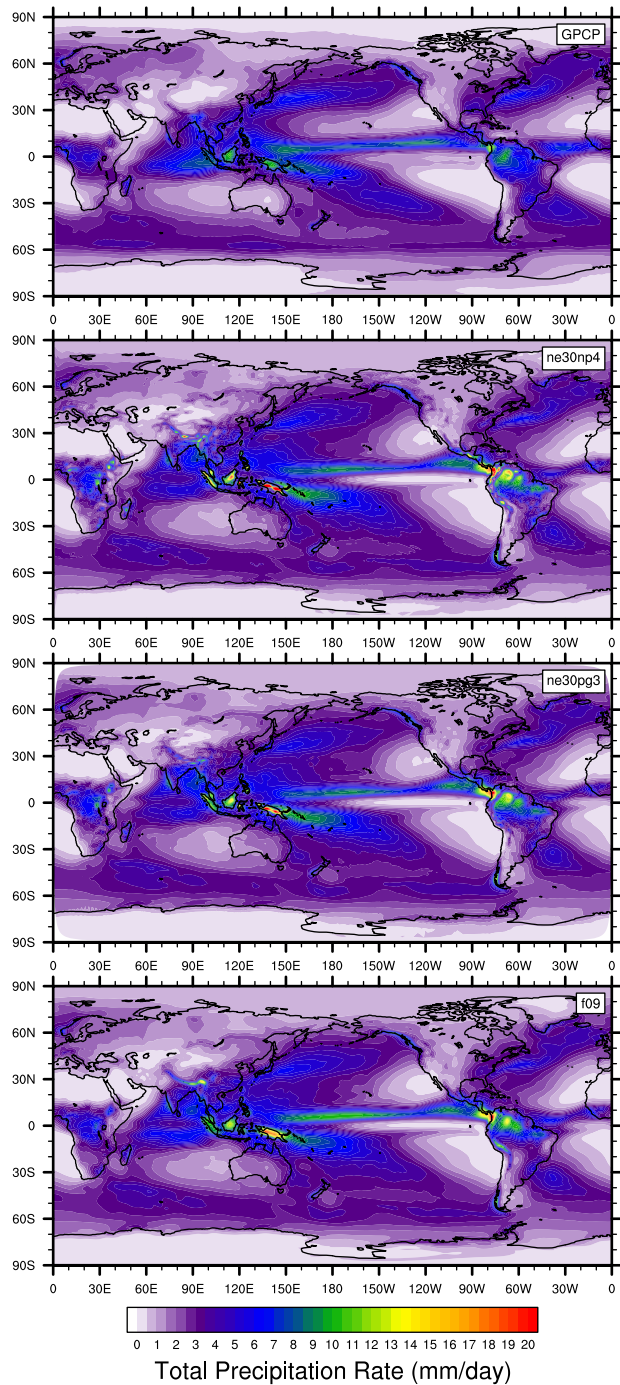
574 FIG. 9. Mean (left) and variance (right) of the low level temperature tendencies from the physical parameter-
 575 izations on the GLL grid, with the *ne30np4* configuration, (top row) and *ne30pg3* configuration (bottom row),
 576 in a pair of year-long aqua-planet simulations after ?. Grid imprinting is observed along the element boundaries
 577 in *ne30np4*, but is absent from the *ne30pg3* simulation.



578 FIG. 10. Mean ω at two model levels in the middle troposphere, in a Held-Suarez configuration outfitted with
 579 real world topography. (Left) CAM-SE state on the GLL grid, *ne30np4*, (Middle) CAM-SE-CSLAM state on
 580 the GLL grid, *ne30np4* and (Right) CAM-SE-CSLAM state on the physics grid, *ne30pg3*. The ω fields are
 581 computed from a 1200 day Held-Suarez simulation. The data are contoured according to a ‘cell fill’ approach,
 582 in which the coupler grids (e.g, Figure 4) are used to delineate the vertices of the control volumes.



583 FIG. 11. Climatological total precipitation rate (in mm/day) computed from the final 19 years of a pair of 20
 584 year long AMIP type simulations. (Left) CAM-SE, (middle) CAM-SE-CSLAM and (Right) their differences.
 585 The difference field is computed through bilinearly interpolating to a common latitude-longitude grid.



586 FIG. 12. Climatological total precipitation rate computed from the final 19 years of a suite of 20 year long
 587 AMIP simulations, using CAM-SE (ne30np4), CAM-SE-CSLAM (ne30np3) and CAM-FV (f09). The top plot
 588 is an observational product, the gridded GPCP climatological precipitation dataset.

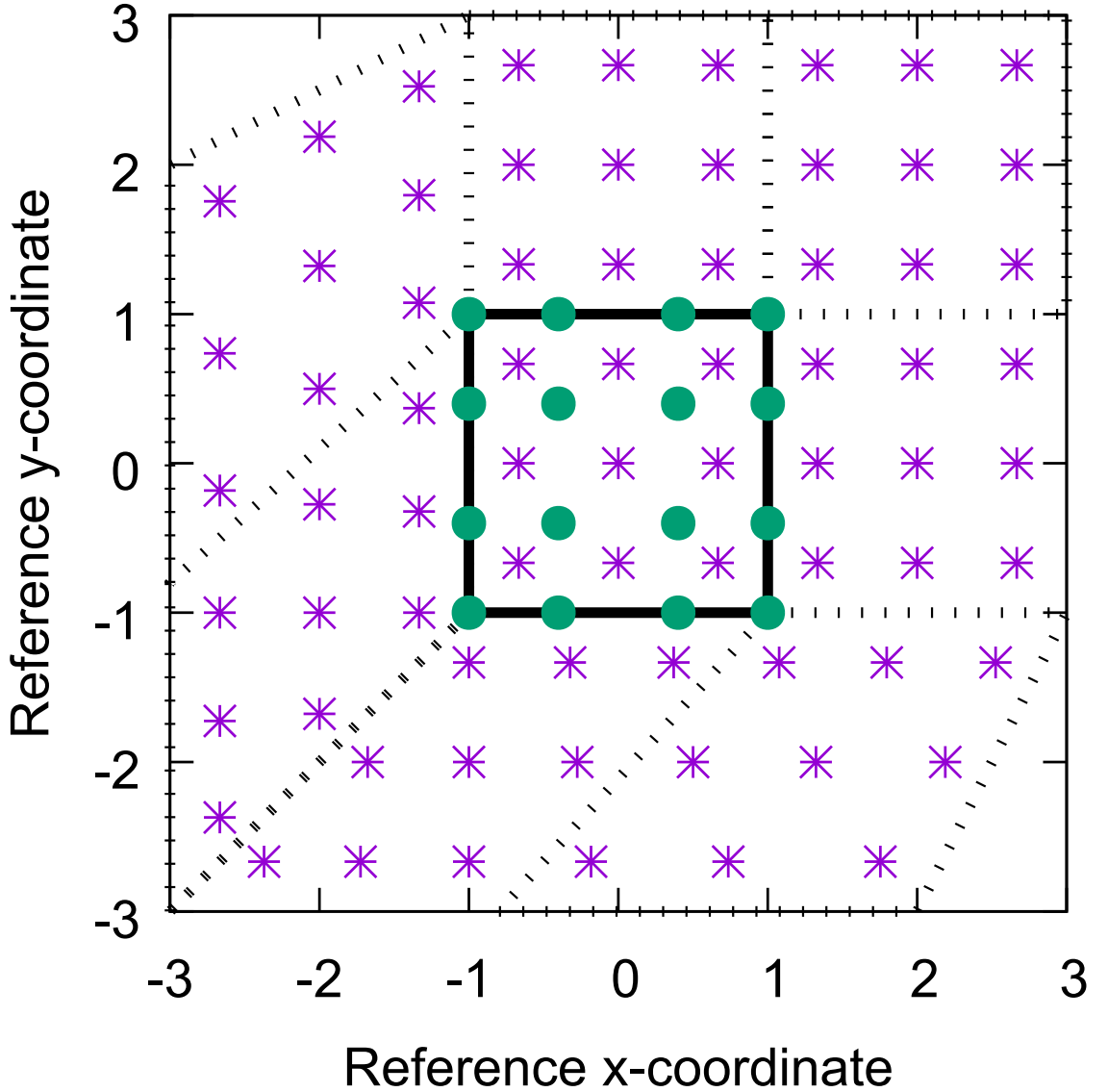


FIG. 13. Schematic of the coordinate system in which the dimensionally split cubic Lagrange interpolation is computed. The physics grid centers are marked with asterisks and the GLL points, we are interpolating to, with solid filled circles. The element in which the GLL points are located is bounded by thick black lines and located in the lower left corner of a panel. The stippled lines mark the boundaries of the remaining elements. For simplicity we are using the normalized coordinate centered at the element on which the GLL points we are interpolating to are located. Note that the coordinates for points on neighboring panels (using a different local coordinate system) must be transformed to the coordinate system of the element in question.